

# Eliminating the Barriers: Demystifying Wi-Fi Baseband Design and Introducing the PicoScenes Wi-Fi Sensing Platform

Zhiping Jiang, Tom H. Luan, Xincheng Ren, Dongtao Lv, Han Hao, Jing Wang, Kun Zhao, Wei Xi, Yueshen Xu, and Rui Li

arXiv:2010.10233v2 [cs.AR] 11 Mar 2021

**Abstract**—Over the past decade, research on Wi-Fi sensing has been thriving but not smooth. Three barriers severely hamper related research, namely, unknown baseband design and its influence on channel state information (CSI), inadequate hardware and the lack of versatile and flexible measurement software. This paper aims to eliminate them through the following work. *First*, we present an in-depth study of the baseband design of the Qualcomm Atheros AR9300 (QCA9300) NIC. Based on this study, we identify a critical missing item in the existing CSI model, namely, the CSI distortion, and identify the baseband filter as its origin. We also propose a trivial distortion removal method. *Second*, we reintroduce both the QCA9300 and software-defined radio (SDR) as the best hardware for research. For the QCA9300, we unlock over-GHz spectrum access by achieving arbitrary tuning of both the carrier frequency and bandwidth. For SDR, we develop a software implementation of the Wi-Fi baseband, allowing users to fully control the baseband and access the complete physical-layer information. *Third*, we release the PicoScenes software. It supports multi-NIC concurrent operation of QCA9300, Intel Wireless Link (IWL5300) and SDR hardware. It features packet-injection-based transmission, low-level control, and software baseband implementation. It also allows users to develop their own measurement-specific plugins. Finally, we report extensive evaluations of the PicoScenes system. Many of the results are groundbreaking, such as concurrent CSI measurement on a 27-NIC array, a CSI measurement rate of up to 40 kHz on the QCA9300, 1 kHz CSI measurement rate on SDR and 200 MHz-bandwidth CSI measurement on SDR.

**Index Terms**—Wi-Fi Sensing, CSI Distortion, Baseband Design, Wi-Fi Baseband, PicoScenes, SDR, CSI Measurement.

## I. INTRODUCTION

After a decade of advancement, channel state information (CSI)-based Wi-Fi sensing has grown into a thriving and fruitful research field and has led to new areas of sensing research, such as passive gesture recognition [1] [2] [3], motion tracking [4], respiration detection [5] [6], through-wall detection [7], and sign language recognition [8] [9]. However, the 10-year evolution of Wi-Fi sensing research has not been smooth and has been hampered by the following three barriers:

Zhiping Jiang, Xincheng Ren, Dongtao Lv, Jing Wang, Yueshen Xu and Rui Li are with the School of Computer Science and Technology, Xidian University, Xi'an, China. Email: {zpj, ysxu, rli}@xidian.edu.cn, {xcren, tdlv, jingwang\_buer}@stu.xidian.edu.cn.

Tom H. Luan is with the School of Cyber Engineering, Xidian University, Xi'an, China. Email: tom.luan@xidian.edu.cn.

Han Hao, Kun Zhao and Wei Xi are with the School of Computer Science and Technology, Xi'an Jiaotong University, Xi'an, China. Email: {kunzhao, xiwei}@xjtu.edu.cn, {haohan9717}@stu.xjtu.edu.cn.

Rui Li is the corresponding author.

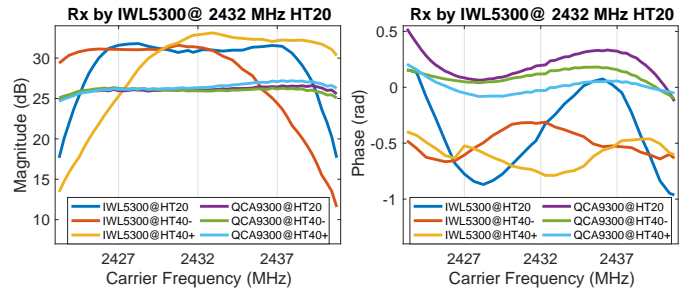


Fig. 1. CSI measurement (magnitude and phase response) conducted in a radio-anechoic chamber. Two Tx ends, QCA9300 and IWL5300 NICs, injected packets at 2432 MHz with HT20 and HT40+/- channel modes. The Rx end, an IWL5300 NIC, operated at 2432 MHz with HT20 channel mode. The magnitude shows M-shaped and half M-shaped response, and the phase shows horizontal S-shaped response.

**Barrier 1: Unknown baseband design and its influence on CSI.** In the Wi-Fi sensing research field, the widely adopted CSI model [10], [11] can be simplified as follows.

$$\mathbf{Y} = \mathbf{H}_{bb} \cdot \mathbf{X} + \mathbf{N} \quad (1)$$

$$\mathbf{H}_{bb} = \mathbf{H}_{air} \cdot \mathbf{H}_{\theta} \quad (2)$$

Here, (1) describes how the baseband channel frequency response (CFR)  $\mathbf{H}_{bb}$ , or the CSI usually obtained via CSI tools, transforms the baseband signal  $\mathbf{X}$  into the received form  $\mathbf{Y}$  with some acceptable noise  $\mathbf{N}$ . (2) describes how, in the context of Wi-Fi sensing research,  $\mathbf{H}_{bb}$  is further decomposed into two terms,  $\mathbf{H}_{air}$  and  $\mathbf{H}_{\theta}$ .  $\mathbf{H}_{air}$  denotes the pure *in-air* channel response, which, under ideal conditions, characterizes the complete *in-air* signal propagation, including the multipath effect, distance fading, the Doppler effect, *etc*. The second term,  $\mathbf{H}_{\theta}$ , is used to denote the sum of all types of phase errors, including but not limited to the carrier frequency offset (CFO), sampling frequency offset (SFO), symbol timing offset (STO) and sampling clock offset (SCO).

The above model ignores the influence of hardware. Because hardware specifications are kept secret to the public, researchers have no option but to believe the influence of hardware to be weak and relatively flat. This belief is reasonable because the Wi-Fi standard indeed imposes stringent restrictions on spectral flatness and spectral masking [12].

However, *real-world evaluations indicate a quite different situation*. We placed an Intel WiFi Link 5300 (IWL5300)

network interface controller (NIC) and a Qualcomm Atheros AR9300 (QCA9300) NIC in a radio anechoic chamber and measured the CSI between them. Since such a chamber suppresses the multipath effect and frequency-selective fading in the frequency domain, we anticipated smooth and flat CSI measurements. However, as shown in Fig. 1, the results showed strong nonflatness in both magnitude and phase. Especially in the HT40+/- cases, the differences in magnitude among the subcarriers were even greater than 15 dB. We repeated the measurements in a wide variety of position, carrier frequency and bandwidth configurations and confirmed the same results. This strong nonflatness is obviously *beyond the scope of hardware imperfection*. The only possible explanation is that **an unknown CSI distortion** exists in the transmitter (Tx) and/or receiver (Rx) process. This distortion, when properly considered, may affect nearly all Wi-Fi sensing research, and it *fundamentally challenges the correctness of the above CSI model*. To address this situation, three important questions must be answered:

- What is this distortion, and where does it come from?
- Can we alter the known modes to fit this distortion?
- How can we eliminate this distortion?

**Barrier 2: Inadequate hardware.** After years of flourishing development, Wi-Fi sensing research is now impeded by hardware challenges, which are reflected in three aspects.

First, there is an *inability to provide advanced hardware features*, which is the downside of the double-edged sword of low-cost design. The hardware of all existing CSI tools [13], [14], [15] is designed for low-cost mobile Wi-Fi connections; therefore, their compact and low-cost physical designs mean that they lack many advanced hardware features, some of which are greatly desired in Wi-Fi sensing, such as the ability to use more than three radio chains or externally supplied clock sources and phase synchronization across antennas.

Second, *low-level hardware control* is unavailable. Beyond the working channel, channel mode and transmit power, the existing CSI platforms provide almost no low-level control. The lack of low-level control, such as tuning of the carrier frequency and sampling rate, radio-frequency (RF) calibration, in-phase/quadrature (I/Q) mismatch [16], and automatic gain control (AGC), has not only limited the innovation space of Wi-Fi sensing research but also eliminated the chance to further explore hardware design.

The third problem is the *inaccessibility of other valuable physical (PHY)-layer information*. CSI is just one of the most appealing types of PHY-layer information that the hardware baseband produces. During packet decoding, the baseband also generates, for example, CSI measured from the legacy long training field (L-LTF), CFO and SFO information measured from the digital baseband, equalized orthogonal frequency-division multiplexing (OFDM) symbols, etc. However, existing CSI tools return only the CSI measured from the high-throughput LTF (HT-LTF).

As an alternative to commercial off-the-shelf (COTS) Wi-Fi NICs, software-defined radio (SDR) is becoming popular in Wi-Fi sensing research due to its attractive capability of total control over all low-level details [17], [18], [19], [20].

However, a dilemma arises in applying SDR devices in Wi-Fi sensing research. On the one hand, the lack of a publicly available baseband implementation that is at least compatible with the 802.11n protocol is a considerable obstacle; on the other hand, to the best of our knowledge, very few teams have developed their own implementations. Part of the reason is that developing an 802.11n-compatible software baseband is a challenging project, sometimes more difficult than Wi-Fi sensing research itself.

**Barrier 3: The lack of versatile and flexible measurement software.** In addition to inadequate hardware, the companion software, including modified drivers, poses a hindrance to research. The lack of multi-NIC CSI measurement support is a difficult obstacle to overcome when building a COTS NIC-based phased array [21]. The lack of measurement metadata, such as the source address, injection tracking number and session ID, presents difficulties for the alignment and pre-processing of raw CSI measurements. In addition, there are growing demands for the ability to perform various advanced CSI measurements, such as real-time collaborative measurements between a Tx and Rx, high-speed round-trip measurements and synchronized channel scanning [22]. To meet these goals, software should support both frame injection and real-time in situ CSI parsing and processing; however, the existing tools do not provide Tx and Rx control or a CSI data parsing library. Finally, the variability of sensing tasks expects software to be flexible to allow researchers to prototype their research-specific sensing tasks quickly. Unfortunately, the existing software is architecturally too simple to meet this goal.

This paper aims to address the above barriers in three goals.

To eliminate Barrier 1, we piece together a detailed architecture for the baseband design for the QCA9300 NIC. This detailed architecture covers the RF frontend, analog baseband, and digital baseband. We study in detail three of the most important components: the register-based control mechanism, dual-band carrier frequency synthesis and baseband multirate clocking. Then, we evaluate the impact of a wide variety of baseband configurations on the CSI distortion and identify the baseband, especially baseband filtering, as the most influential factor. The evaluations also indicate that CSI distortion is pervasive in all Wi-Fi NICs, including IWL5300, QCA9300 and even SDR devices. Finally, we propose a trivial method of measuring and eliminating CSI distortion.

To eliminate Barrier 2, we achieve remarkable breakthroughs in both the COTS Wi-Fi NIC and SDR directions. First, as an additional benefit of QCA9300 baseband exploration, we unlock some of its most valuable low-level features, such as arbitrary tuning of both the carrier frequency and the baseband sampling rate, Tx/Rx radio chain selection and per-packet multi-CSI measurement. Second, to solve the aforementioned dilemma of SDR, we develop a high-performance software baseband implementation for the 802.11a/g/n/ac/ax protocols, which enables the user to precisely tune a wide range of low-level details, such as the bandwidth, packet timing, CFO, SFO, spatial mapping, resampling, and even Tx/Rx I/Q mismatch. In addition to such low-level control, another advantage is the *availability of complete PHY-layer information*. In addition to the commonly available CSI, it

provides the CSI measured from the L-LTF, CFO estimation, the scrambler initial value, and even the raw baseband signal.

To eliminate Barrier 3, we develop and release PicoScenes, a versatile and flexible Wi-Fi sensing platform software. PicoScenes integrates packet injection, in situ parsing of CSI data, and low-level hardware control for all supported hardware, including QCA9300, IWL5300 and SDR devices. *PicoScenes on SDR*, which provides dedicated support for SDR devices, integrates the high-performance baseband implementation between the unified hardware abstraction and SDR driver. In this way, it enables SDR devices to transmit and receive standard-compatible Wi-Fi packets in real time, similar to ordinary COTS Wi-Fi NICs. PicoScenes also supports multi-NIC concurrent operation, such as concurrent CSI measurement and in situ CSI data parsing. Regarding the flexibility of the architecture, we provide a rich set of user-friendly and hardware-unified application programming interfaces (APIs), which enable users to quickly prototype their own measurement plugins. Finally, as a demonstration of this architecture, we develop EchoProbe, a PicoScenes-based CSI measurement plugin. It provides *ms*-grade round-trip CSI measurement and spectrum scanning capabilities.

Our contributions are summarized as follows:

First, we eliminate the barrier of unknown baseband design by presenting an in-depth study of the baseband design of the QCA9300. To the best of our knowledge, this is the first study of hardware baseband design for Wi-Fi NICs and its influence on CSI since the emergence of CSI-based Wi-Fi sensing research. We identify the pervasiveness of CSI distortion and propose a reliable solution for eliminating this distortion. The baseband design knowledge gained from the QCA9300 is of great guiding significance for inferring how other confidential platforms operate, such as the IWL5300 and the Broadcom 43xx (BCM43xx) series [15].

Second, we eliminate the barrier of inadequate hardware to a significant extent by reintroducing both the QCA9300 and SDR as the best hardware for Wi-Fi sensing. For the QCA9300, we achieve arbitrary tuning of both the carrier frequency and the baseband sampling rate. To the best of our knowledge, this is the first work that provides *over-GHz continuous spectrum access for a COTS Wi-Fi NIC*. For SDR devices, PicoScenes on SDR facilitates Wi-Fi sensing research by *packaging the three best features together*: COTS NIC-like real-time CSI measurement, complete low-level hardware control and the provision of the complete PHY-layer information. We believe that with this platform, the dilemma previously faced when adopting SDR devices in Wi-Fi sensing research is now completely resolved.

Third, we eliminate the barrier of the lack of measurement software by releasing the PicoScenes Wi-Fi sensing platform, an immediately downloadable supercharger for Wi-Fi sensing research. PicoScenes provides extensive architectural versatility and flexibility to support the next wave of Wi-Fi sensing research. It features concurrent CSI measurement from multiple NICs and easy access to the unlocked features of the QCA9300 and IWL5300. PicoScenes on SDR provides dedicated support for SDR devices, allowing users to fully control the low-level details and access much richer PHY-layer information than is

possible with COTS Wi-Fi NICs. PicoScenes also encapsulates low-level hardware controls into user-friendly APIs, which are then made available to the application- or measurement-specific plugin layer. As a result, users can quickly prototype their own measurement plugins while avoiding engagement with cumbersome low-level details.

Finally, comprehensive evaluations demonstrate the feasibility and high performance of PicoScenes. Many of the results are state of the art, such as up to 2.4 GHz wide full-spectrum availability for the QCA9300, the release of a reference design for a 27-NIC array, the sub-*ms*-grade baseband signal generation and decoding functionality of PicoScenes on SDR, and 10 kHz (real-time mode) and 40 kHz (replay mode, reaching the theoretical limit) packet injection and CSI measurement capabilities. Finally, we support *reproducible* research by releasing the test code within the installation package for the PicoScenes software.

The rest of this paper is organized as follows. Section II briefly reviews recent works on Wi-Fi sensing. Section III presents an in-depth study of the baseband design of the QCA9300. Section IV deeply investigates the CSI distortion. Section V introduces the PicoScenes Wi-Fi sensing system. Section VI reports extensive evaluations of PicoScenes. Finally, Section VIII concludes the paper.

## II. RELATED WORK

Remarkable advancements in Wi-Fi sensing [10] have been achieved over 10 years of development, leading to many new areas of research related to fine-grained sensing, such as indoor localization [23], [24], [25], [26], [27], [19], [28], trajectory tracking [29], [30], [31], material identification [32], hand gesture recognition [33] and location-based security [34], [35], [36]. mDTrack [19] relies on a joint approach to simultaneously estimate the angle of arrival (AoA), time of flight (ToF) and Doppler effect, achieving decimeter-level resolution for indoor localization. Nopphon *et al.* [29] extracted the Doppler frequency from CSI and used it to track a hand trajectory with centimeter-level accuracy. WiMi [32] is a sophisticated system that can identify the type of a material regardless of its motion state. WiWrite [33] observes the different signal reflection patterns caused by different hand gestures and uses them to realize precise character recognition and word estimation. RIM [28] is a recently proposed system focusing on inertial measurement for tracking movement distance, heading direction and rotation angles. It leverages the phase difference between antennas to infer the movement direction and speed.

Regarding the hardware used in related research, the IWL5300 is the most widely used NIC for CSI extraction [25], [31], [28]. This NIC works with common laptops and allows users to easily carry out CSI measurements. The second most popular NIC is the QCA9300 [14], [37], [28], which reports CSI with 10-bit resolution and uncompressed subcarriers. However, the Atheros CSI Tool prioritizes the development of router versions, making it less convenient for Wi-Fi sensing. The Nexmon Channel State Information Extractor [15], [38] is the latest entry in the list of available CSI-ready devices. It is based on a BCM43xx series chip, such as those equipped on

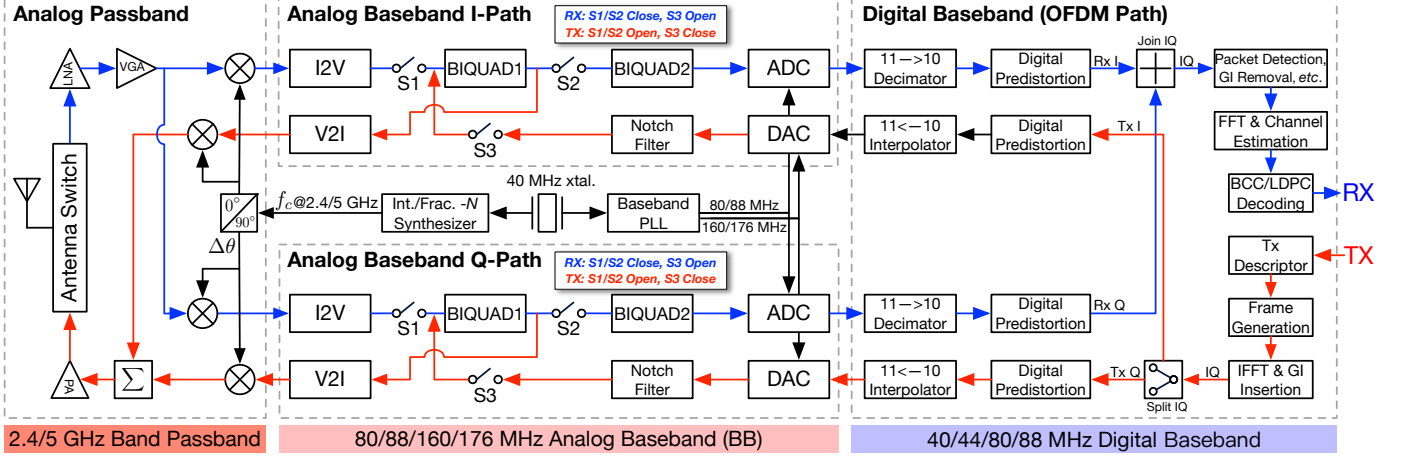


Fig. 2. QCA9300 transceiver architecture. The TX and Rx processing flows are highlighted in red and blue, respectively.

several Android smart phones, Raspberry Pi models, and Wi-Fi routers. The inability to access low-level hardware control is a barrier to more advanced Wi-Fi sensing research; however, SDR-based CSI extraction is even more difficult [17], [18], [20]. Universal Software Radio Peripheral (USRP) devices, the Wireless Open-Access Research Platform (WARP) and other SDR hardware devices are merely RF frontends, and the lack of a Wi-Fi software implementation is a fatal problem.

Regarding the hardware used in the research, IWL5300 is the most widely used NICs for CSI extraction [25], [31], [28]. This NIC works with common laptop and user can carrier out CSI-measurement easily. The second is QCA9300[14], [37], [28], which reports CSI with 10-bit resolution and uncompressed subcarriers. However, Atheros CSI Tool prioritizes the development of router version, which is less convenient for Wi-Fi sensing. Nexmon CSI Extractor [15], [38] is the latest update to the list of CSI-ready devices. It is based on Broadcom 43xx series chip, which has be equipped in several Android smart phones, Raspberry models, and some Wi-Fi Routers. The inability to access the low-level hardware control is a barrier to more advanced Wi-Fi sensing research, however, SDR-based CSI extraction is even harder[17], [18], [20]. SDR hardware are merely the RF frontend, and the lack of the Wi-Fi software implementation is the key problem.

### III. QCA9300 HARDWARE ARCHITECTURE

In this section, we describe the hardware design of the QCA9300 NIC. We first present the general architecture, and then we focus on 3 specific design features that are valuable for Wi-Fi sensing applications and research. Finally, we briefly discuss what we can learn from the QCA9300 and draw conclusions about how other Wi-Fi NICs operate.

#### A. The Architecture of QCA9300

The detailed baseband design is the key to examining Wi-Fi hardware and revealing the process that the signal undergoes. Unfortunately, this information is kept confidential and not released to the public, and all CSI-ready COTS NICs

are subject to similar technical confidentiality requirements, including the IWL5300, QCA9300 and BCM43xx NICs.

Fortunately, Atheros has published several enlightening papers regarding the detailed design of their 802.11n Wi-Fi chips [39], [40], [41], [42]. Based on these public documents and our in-depth study of the open-source driver of the QCA9300 (codenamed *ath9k* [43]), we have pieced together a detailed understanding of the QCA9300 baseband design, as shown in Fig. 2. For simplicity, this diagram shows only one of the three transceiver chains and focuses on the frontend design. The baseband consists of several key components, namely, the *Digital Baseband*, *Analog Baseband*, and *Analog Passband*.

The *Digital Baseband* mainly concerns issues related to Wi-Fi baseband encoding/decoding, such as fast Fourier transform (FFT) and inverse FFT (IFFT) pairs, packet detection, CSI measurement, OFDM modulation/demodulation, binary convolutional coding (BCC)/low-density parity-check (LDPC) codecs, windowing, and interleaving.

On the boundary between the digital baseband and the analog baseband are two pairs of analog-to-digital converters (ADCs) and digital-to-analog converters (DACs), which sample in-phase and quadrature signals separately.

The *Analog Baseband* mainly performs sampling and filtering. A 40 MHz crystal oscillator drives the baseband phase-locked loop (PLL), which feeds different frequencies to the DACs and ADCs, both of which are several times higher than the signal bandwidth. This somewhat strange clocking plan is discussed in detail below. Both BIQUAD1 and BIQUAD2 are active-RC-based low-pass filters (LPFs) with run-time reconfigurability, and BIQUAD1 is shared between the Tx and Rx paths. On the Tx path, the notch filter, BIQUAD1 and voltage-to-current converter (V2I) form a second-order Butterworth filter. This filter serves as a reconstruction filter that removes the spectral images created by the DAC. On the Rx path, the current-to-voltage converter (I2V), BIQUAD1 and BIQUAD2 form a fifth-order Butterworth filter. This filter is primarily used as a pre-ADC anti-aliasing filter but also serves as an adjacent channel rejection (ACR) filter.

The *Analog Passband* is primarily responsible for carrier frequency synthesis, up-/downconversion, power amplification

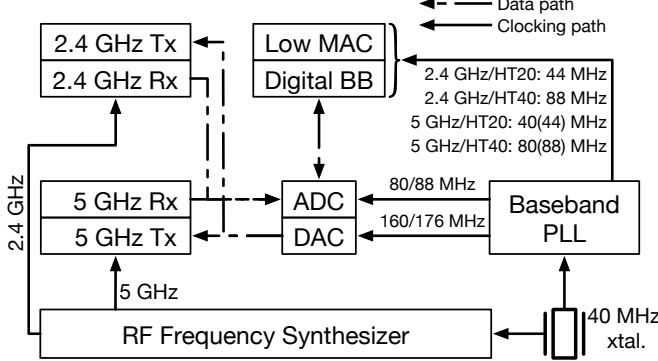


Fig. 3. Clocking hierarchy of the QCA9300. The 40 MHz crystal gives rise to two clocking branches. RF Frequency Synthesizer generates the carrier frequencies, while Baseband PLL generates multiple matched clocks for the baseband components. The values in parentheses are the frequencies when the *fastclock* option is on.

on the Tx and Rx paths, and antenna switch control. The QCA9300 uses a single synthesizer to generate the carrier frequencies for both the 2.4 and 5 GHz bands. This design is discussed in further detail below.

#### B. Major design highlights of the QCA9300

In this section, we discuss three of the most relevant design features for Wi-Fi sensing.

1) *Highly configurable soft-MAC architecture*: The QCA9300 is a NIC with *soft* medium access control (MAC), *i.e.*, the *ath9k* driver has complete control over the NIC via a large number of control registers exposed by the hardware. For instance, the Atheros CSI Tool [14] forces the hardware to report the per-packet CSI by assigning 1 to the 28th bit (*H\_TO\_SW\_DEBUG\_MODE*) of the control register 0x8344 (*AR\_PCU\_MISC\_MODE2*). Notably, these registers can also be accessed indifferently by user-space programs, which allows the PicoScenes software to directly control the hardware. Taking advantage of this feature, PicoScenes exposes a number of valuable hardware controls through public APIs, enabling modifications such as arbitrary tuning of the carrier frequency and sampling rate, as detailed below.

2) *Wide-range and user-tunable baseband clocking*: The clocking architecture, as shown in Fig. 3, is one of the most critical design features of the QCA9300. The 40 MHz local oscillator (LO), denoted by ‘40 MHz xtal.’ in the figure, has two branches. One goes into Baseband PLL to drive the entire baseband, and the other is fed into RF Frequency Synthesizer to generate the carrier frequencies for both the 2.4 GHz and 5 GHz bands. We focus on the baseband branch first.

The 802.11n baseband encodes and decodes a Wi-Fi baseband signal with a 20 MHz or 40 MHz bandwidth; we denote this frequency by  $f_{sig\_bb}$ . However, the actual baseband clocking process involves much more than only two operating frequencies. As shown in Fig. 3, Baseband PLL generates a group of matched clocks that drive different parts of the baseband circuit. Even more confusingly, many of the frequencies have another “paired” frequency that is 1.1 $\times$  higher, such as 80/88 MHz and 160/176 MHz. The reasons behind this complex design are worth knowing.

TABLE I  
QCA9300 BANDWIDTHS CALCULATED FROM PARAMETER QUADRUPLES

(DIV_INT, REF_DIV, CLK_SEL)	HT_2040 = 0	HT_2040 = 1
(22, 10, 1)	2.5 MHz	5 MHz
(22, 10, 0)	5 MHz	10 MHz
(22, 5, 1)	5 MHz	10 MHz
(22, 5, 0)	10 MHz	20 MHz
(33, 5, 0)	15 MHz	30 MHz
(44, 5, 0)	20 MHz	40 MHz
...	...	...
(88, 5, 0)	40 MHz	80 MHz

There are three main challenges motivating this clocking design. The first is the need to overcome the imperfections of the DAC in the Tx baseband. A DAC, by its very nature, cannot perfectly reconstruct analog signals because the produced stair-step waveform creates both in-band *sinc* fading and out-of-band spectral “images” [44] which repeat the in-band signal spectrum at every multiple of the sampling rate. These two types of distortion violate both the spectral flatness and spectral masking requirements specified in the 802.11 standard [45]. To remove these spectral images, a reconstruction filter must follow the DAC. If the DAC samples the signal at 20 MHz, only a 10 MHz transition zone is left for the reconstruction filter; therefore, a high-order filter is needed to suppress the images. However, a high-order filter is expensive in an integrated circuit (IC) design because it leads to both a large IC area and high power consumption.

The QCA9300 addresses this problem via oversampling. In the QCA9300, the DAC operates at 160 MHz, 8x higher than the 20 MHz signal bandwidth. According to sampling theory [44], 8x oversampling stretches the sinc fading by 8x and has two benefits: first, the in-band spectrum is smoothed and therefore meets the spectral flatness requirement; second, 8x oversampling also results in an 8x stretched transition zone, which permits the use of a lower-order filter. Finally, as shown in Fig. 2, the combination of a second-order LPF and a notch filter is sufficient to suppress the spectral images.

The second challenge is the power consumption. Running the entire baseband at 160 MHz is unnecessary and would be inefficient in terms of power. Instead, to achieve a trade-off between power efficiency and signal performance, the baseband PLL generates 3 levels of subfrequencies. The Tx DAC runs at the highest frequency, *i.e.*,  $f_{tx\_dac}=160$  MHz; the Rx ADC runs at the intermediate frequency, *i.e.*,  $f_{rx\_adc}=80$  MHz; and the digital baseband runs at the lowest frequency, *i.e.*,  $f_{digi\_bb}=40/80$  MHz, depending on whether the HT20 or HT40/- channel mode is used.

The third challenge is to achieve backward compatibility with the 802.11b protocol. In the 2.4 GHz band, the NIC needs to support the 802.11b/g/n protocols simultaneously. However, the 22 MHz signal bandwidth of the 802.11b protocol, *i.e.*,  $f_{sig\_bb} = 22$  MHz, is not compatible with either the 20 or 40 MHz signal bandwidth of the 802.11 g/n protocol.

The QCA9300 adopts a multirate design to simultaneously accommodate the 802.11b/g/n protocols in the 2.4 GHz band [40], [42]. To this end, the QCA9300 boosts  $f_{digi\_bb}$ ,  $f_{rx\_adc}$ , and  $f_{tx\_dac}$  by 1.1 $\times$  to 44, 88, and 176 MHz, re-

spectively. For the 802.11b case, the bandwidth gap between  $f_{digi\_bb} = 44$  MHz and  $f_{sig\_bb} = 22$  MHz is bridged by a pair consisting of a  $1/2x$  frequency divider and a  $2x$  frequency multiplier. For the 802.11n HT40+/- case, as shown in Fig. 2, the QCA9300 uses a  $10 \leftrightarrow 11$  sequencing interpolator/decimator pair to bridge the gap between  $f_{digi\_bb} = 44$  MHz and  $f_{sig\_bb} = 40$  MHz. For the 802.11g or 802.11n HT20 case, *i.e.*, for  $f_{sig\_bb} = 20$  MHz signals, QCA9300 still treats them as 40 MHz signals and samples them with  $f_{digi\_bb} = 44$  MHz but later discards half of the subcarriers in an interleaved manner. Finally, in the 5 GHz band, the QCA9300 bypasses the  $10 \leftrightarrow 11$  sequencing interpolator and decimator and restores  $f_{digi\_bb}$ ,  $f_{rx\_adc}$ , and  $f_{tx\_dac}$  to 40, 80, and 160 MHz, respectively. It is worth noting that in some later models of the QCA9300, such as the QCA9380/9390/9590, there is a *fastclock* option (ON by default) that specifies the 44/88/176 MHz clocks for both the 2.4 and 5 GHz bands.

Regarding the control mechanism,  $f_{digi\_bb}$ ,  $f_{rx\_adc}$  and  $f_{tx\_dac}$  are collectively derived from the core baseband PLL clock, denoted by  $f_{pll}$ . ath9k uses a parameter quadruple to tune  $f_{pll}$ . This parameter quadruple has the form (DIV\_INT, REF\_DIV, CLK\_SEL, HT20\_40). These parameters represent the *integer multiplier*, the *reference clock divider*, *clock selection* and *channel mode selection*, respectively. Through some reverse engineering, we have learned how to tune  $f_{pll}$  and the derived clocks, as follows:

$$f_{pll} = \text{DIV\_INT} \times \frac{f_{xtal.}}{\text{REF\_DIV}} \times \frac{2^{\text{HT20\_40}}}{2^{(2+\text{CLK\_SEL})}}, \quad \text{CLK\_SEL} \in \{0, 1, 2\}, \quad \text{HT20\_40} \in \{0, 1\} \quad (3)$$

$$f_{rx\_adc} = f_{pll} \quad (4)$$

$$f_{tx\_dac} = 2 \cdot f_{pll} \quad (5)$$

$$f_{digi\_bb} = 1/2 \cdot f_{pll} \quad (6)$$

$$f_{sig\_bb} = 10/11 \cdot f_{digi\_bb} \quad (7)$$

where  $f_{xtal.} = 40$  MHz is the frequency of the core crystal oscillator. In the 2.4 GHz band, the parameter quadruples for the 802.11n HT20 and HT40 modes are (44, 5, 0, 0) and (44, 5, 0, 1), respectively. By substituting these values into Equation (3), we obtain a value of 88 MHz or 176 MHz for  $f_{pll}$  and values of 20, 44, 88 and 176 MHz or 40, 88, 176 and 342 MHz for  $f_{sig\_bb}$ ,  $f_{digi\_bb}$ ,  $f_{rx\_adc}$  and  $f_{tx\_dac}$ , respectively. As is clear from the above equations, the baseband PLL clock  $f_{pll}$  controls the pace of the entire baseband; therefore, tuning  $f_{pll}$  is equivalent to tuning the channel bandwidth. Table I lists the channel bandwidths calculated from several parameter quadruples. Although this list is incomplete, it is still surprising that on the bandwidth of QCA9300 can be scaled from a minimum of 2.5 MHz up to 80 MHz. PicoScenes offers an integrated bandwidth tuning functionality for the QCA9300, allowing users to specify the bandwidth using only a single parameter, “*–rate*”.

3) *Wide-range and user-tunable carrier frequency synthesizer:* As shown in Fig. 4, the QCA9300 uses a shared frequency synthesizer to generate the carrier frequency for both the 2.4 GHz and 5 GHz bands. The frequency synthesizer is a voltage-controlled oscillator (VCO)-based synthesizer with an operating range  $f_{syn}$  from 3.0 GHz to 4.0 GHz.

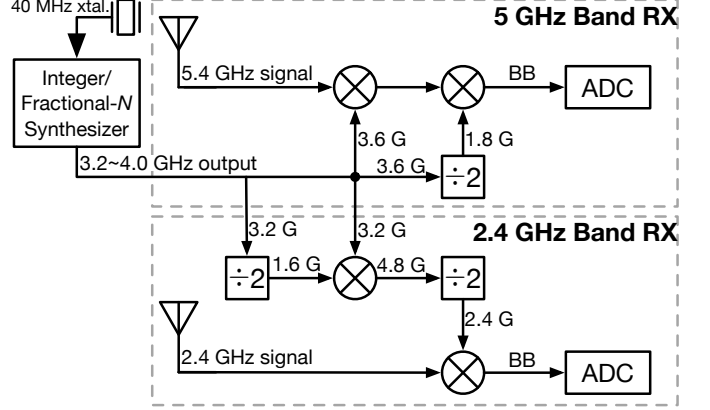


Fig. 4. Carrier frequency synthesis scheme of the QCA9300. An integrated integer/fractional- $N$  synthesizer is shared between the 2.4 and 5 GHz bands but with different frequency conversion paths. For simplicity, this diagram shows only the Rx downconversion path.

TABLE II  
CARRIER FREQUENCIES SUPPORTED BY THE QCA9300

	$f_{syn}$	$f_{rf}^{2.4}$	$f_{rf}^5$
Effectively supported range (GHz)	3.0-4.0	2.2-2.9	4.4-6.1
Minimal tuning resolution (Hz)	305.2	203.3	915.5

The frequency synthesis scheme for the 2.4 GHz band is illustrated in the lower part of Fig. 4. The synthesizer operates near 3.2 GHz, *i.e.*,  $f_{syn} = 3.2$  GHz. To generate a 2.4 GHz band carrier frequency,  $f_{syn}$  is first mixed with half of itself, *i.e.*, 1.6 GHz, producing a 4.8 GHz signal, and the 4.8 GHz signal is divided by 2 to obtain the 2.4 GHz carrier frequency.

The frequency synthesis scheme for the 5 GHz band is illustrated in the upper part of Fig. 4. The synthesizer operates between 3.4 to 3.9 GHz in this band. Taking the downconversion of a 5.4 GHz Rx signal as an example, the synthesizer operates at 3.6 GHz, *i.e.*,  $f_{syn} = 3.6$  GHz. The 5.4 GHz Rx signal is first downconverted to an intermediate frequency (IF) of 1.8 GHz by mixing it with  $f_{syn}$ . Then, the IF signal is downconverted again by mixing it with half of  $f_{syn}$ , *i.e.*, 1.8 GHz. In this way, the signal is dual-converted to the baseband.

Regarding the control mechanism, with some reverse engineering, we have learned how to tune the synthesizer, as follows:

$$f_{syn} = \text{CHANSEL} \times \frac{f_{xtal.}}{2^{17}} \quad (8)$$

$$f_{rf}^{2.4} = 3/4 \cdot f_{syn}, \quad f_{rf}^5 = 3/2 \cdot f_{syn} \quad (9)$$

where CHANSEL is an unsigned integer variable used for tuning  $f_{syn}$  and  $f_{rf}^{2.4}$  and  $f_{rf}^5$  are the output carrier frequencies in the 2.4 and 5 GHz bands, respectively. By substituting CHANSEL=1 into (8), we obtain the minimal tuning step of the synthesizer:  $f_{syn\_step} \approx 305$  Hz. In addition, by substituting the working range of the synthesizer into (9), we obtain Table II, which lists the maximum working ranges and resolutions supported by the QCA9300. The PicoScenes software also includes a carrier frequency tuning functionality for the QCA9300, allowing users to specify the carrier frequency using only a single parameter, “*–freq*”.

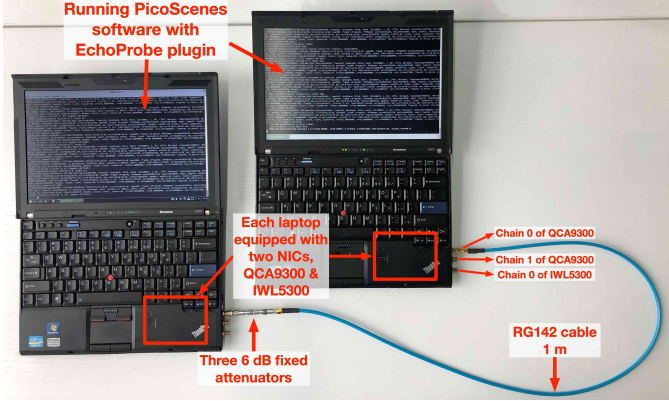


Fig. 5. Hardware setup for CSI distortion evaluation.

### C. What can we learn from the QCA9300?

The QCA9300 provides us with valuable guidance in speculating on how other Wi-Fi NICs operate. Due to the page limit, we discuss only three key points below, which are common to all NICs from all brands and vendors.

The first concerns the influence of the baseband filter. Due to the spectral flatness and masking requirements of the 802.11 standard, all NICs include strong filters before and after the DAC/ADC pair. There is no doubt that these filters exert a certain influence on the in-band signal, including the CSI. Therefore, we may need to re-evaluate the correctness of the CSI model shown in (2), which assumes that the influence of the baseband hardware is merely a linear phase offset.

The second point concerns the sampling time. Phase-based Wi-Fi sensing is sensitive to the STO, which is an integer multiple of the sampling time  $T_s = 1/f_{rx\_adc}$ . Prior works have assumed that the hardware sampling time is equal to the channel bandwidth [10], [11], *i.e.*,  $f_{rx\_adc} = f_{sig\_bb}$ . However, this assumption is not correct, at least for the QCA9300 and the USRP series. For the QCA9300, its Rx ADC operates at 88 and 80 MHz for the 2.4 and 5 GHz bands [40], respectively. For the USRP N210 or X310, both the Tx and Rx run at the master clock rate of 100 or 200 MHz [46], respectively. Even for the IWL5300, based on our preliminary evaluations, we strongly believe that its Rx path operates at 40 MHz.

The third point concerns the CFO. Most modern NICs use integer/fractional- $N$  synthesizers to generate their carrier frequencies. However, as suggested in Equation (8), the synthesizer has a minimum tuning resolution, so the synthesizer cannot be precisely tuned to certain frequencies. Still taking the QCA9300 as an example, if we wish to specify a frequency of 5.2 GHz, the NIC must actually be specified to operate at 5199.999389 MHz or 5200.000305 MHz. This small CFO is perfectly acceptable in Wi-Fi communication and most Wi-Fi sensing applications; however, it may mix with the Doppler effect, contaminating the estimation of the Doppler frequency shift. Unfortunately, the tuning resolution greatly depends on the hardware design, and we currently have detailed clocking architectures only for the QCA9300 and USRP models.

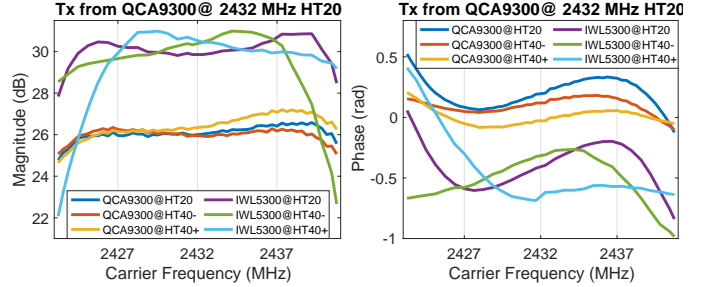


Fig. 6. CSI distortion (magnitude and phase response) under different Rx NIC-channel mode configurations. The Tx end was a QCA9300 NIC continuously injecting packets in the HT20 channel mode. The QCA9300 and IWL5300 installed on the other laptop, both acting as Rx ends, switched among the HT20, HT40+, and HT40- channel modes.

## IV. CHARACTERIZING THE *Pervasive* CSI DISTORTION

In this section, we examine the CSI distortion under various channel configurations and experimentally identify the most likely origin of the distortion. Then, we explain what this distortion is and its cause. Finally, we propose a trivial method of eliminating this distortion.

### A. Where does the CSI distortion come from?

We designed 5 tests to identify the origin of the distortion.

*Test setup:* We used two Lenovo ThinkPad X201 laptops in the tests. They were running the Linux Mint 20 OS (based on Ubuntu 20.04 LTS) with a kernel version of 5.4. The reason for using this old laptop model is that the X201 has two mini PCI-E slots; therefore, we could install both the QCA9300 and IWL5300 NICs on a single laptop. As shown in Fig. 5, the NICs under test were connected by a double-shielded coaxial cable (RG142) and three 6 dB fixed attenuators. During the tests, we used the PicoScenes software to control the injection-based Tx and Rx. We used a low Tx power of 5 dBm to prevent Rx ADC saturation and also shut down the second and third radio chains on the Rx end to prevent undesired maximal ratio combining (MRC).

1) *T1: Test for the influence of the Rx baseband:* In this test, the QCA9300 NIC installed on laptop A injected HT-rate packets at the 2432 MHz channel. Both the QCA9300 and IWL5300 NICs installed on laptop B received the packets in 3 different channel modes, namely, HT20, HT40+, and HT40-. Thus, we tested a total of 6 NIC-channel mode combinations (2 NICs, 3 channel modes). Fig. 6 shows the average magnitude and phase of the received CSI.

Before the analysis, let us briefly review the 802.11n channel modes. HT20 or HT40+/- refers to the 802.11n HT-format channel with 20 or 40 MHz bandwidth, respectively. The bandwidth of HT40+/- channels is doubled to 40 MHz by subsuming an adjacent 20 MHz-bandwidth channel with a higher or lower carrier frequency, and it shifts the carrier frequency toward the center of the merged channels. An HT40+/- channel can also communicate with an HT20 channel by transmitting data on only half of its total subcarriers and filling the other half with 0s. Fig. 6 shows three key observations regarding the distortion.

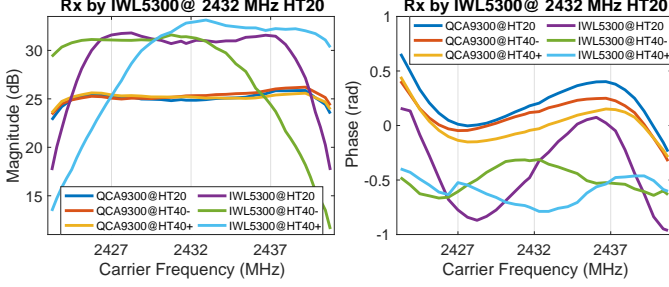


Fig. 7. CSI distortion (magnitude and phase response) under different Tx NIC-channel mode configurations. The Rx end was an IWL5300 NIC operating at 2432 MHz in the HT20 channel mode. A QCA9300 and a second IWL5300, both acting as Tx ends, injected packets in the HT20, HT40+ and HT40- channel modes.

- 1) The CSI difference shown in Fig. 6 can only be attributed to the Rx baseband and the NIC-channel mode configuration because the Tx end and the cable connection remained unchanged during the test.
- 2) In the HT20 channel mode, both NICs exhibit roughly symmetrical distortion. The magnitude and phase show an M-shaped distortion and a horizontal S-shaped distortion, respectively. Both types of distortion are very strong.
- 3) In the HT40+/- channel modes, both the magnitude and phase distortion are heavily biased, especially in the case of the IWL5300. Interestingly, we find that the biased response is similar to a stretched version of the left or right half of the HT20 response.

2) *T2: Test of the influence of the Tx baseband:* In this test, we swapped the Tx and Rx roles. Specifically, the IWL5300 NIC installed on laptop A was used as the Rx NIC<sup>1</sup>. It operated at 2432 MHz in the HT20 channel mode and remained unchanged during the test. The QCA9300 and IWL5300 NICs installed on laptop B transmitted packets in each of the 3 channel modes. Fig. 7 shows the average magnitude and phase of the received CSI. We make the following key observations:

- 1) The CSI difference shown in Fig. 7 can only be attributed to the Tx baseband and the NIC-channel mode configuration because the Rx end and the cable connection remain unchanged during the test. This test actually reveals a long-ignored aspect of Wi-Fi sensing: *the spectrum of the Tx signal actually emitted from the antenna is not flat, either in magnitude or in phase.*
- 2) Given the remarkably high similarity between Fig. 6 and Fig. 7, we speculate that in both NICs, there *may* be one or more shared stages between the Tx and Rx signal flows. The baseband design of the QCA9300 supports this conjecture in that the filter BIQUAD1 is indeed shared between the Tx and Rx flows, as shown in Fig. 2.
- 3) The IWL5300 performs worse than the QCA9300 in terms of spectral flatness and spectral masking. In the HT40+/- cases, the difference in magnitude for the IWL5300 is greater than 10 dB; in contrast, the QCA9300 has better spectral flatness than the IWL5300.

<sup>1</sup>A QCA9300 does not report CSI measurements for packets sent by an IWL5300, but the reverse is possible. Therefore, we used an IWL5300 as the Rx NIC in this test.

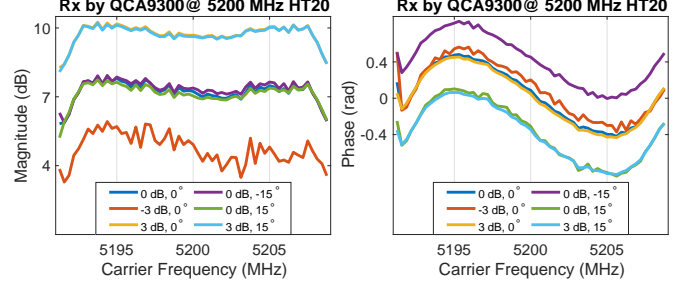


Fig. 8. CSI distortion (magnitude and phase response) under different Rx I/Q mismatch configurations. Both the Tx and Rx ends were QCA9300 NICs operating at 5200 MHz in the HT20 channel mode. On the Rx end, different I/Q mismatch parameters were scanned.

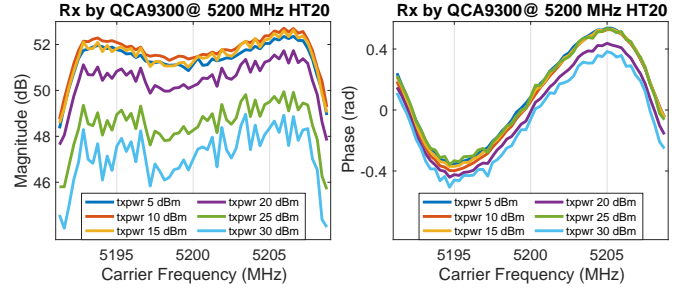


Fig. 9. CSI distortion (magnitude and phase response) under different Tx power levels. Both the Tx and Rx ends were QCA9300 NICs operating at 5200 MHz in the HT20 channel mode. On the Tx end, the transmission power was scanned from 1 to 30 dBm.

3) *T3: Test of the influence of the I/Q mismatch:* I/Q mismatch is a common imperfection of the radio frontend, which is reflected in two mismatches between the in-phase (I) and quadrature (Q) components of the LO signal, namely, *magnitude inequality* and *phase nonorthogonality* [47]. In a previous work [16], it was speculated that the phase distortion may be caused by I/Q mismatch, but this was not verified through experiments.

In this test, we overrode the Rx I/Q imbalance configuration in the ath9k driver and scanned both the I/Q magnitude ratio and the I/Q phase offset of the QCA9300 acting as the Rx end, while the Tx end continuously injected packets at 2432 MHz in the HT20 channel mode. Fig. 8 shows the average magnitude and phase of the received CSI.

Fig. 8 shows that I/Q mismatch creates in-band CSI disturbance and an overall translation of the magnitude; however, both the M-shaped magnitude distortion and the horizontal S-shaped phase distortion remain unchanged. This test proves that I/Q mismatch is *not* associated with the CSI distortion.

4) *T4: Test of the influence of the Tx power:* Similar to the previous test, we used PicoScenes to scan the transmission power on the Tx end. Fig. 9 shows the average magnitude and phase of the received CSI.

It is clear from Fig. 9 that the Tx power is also *not* associated with the CSI distortion. A strange phenomenon is that as the Tx power increases, the CSI magnitude drops. We believe that this is caused by the Rx AGC which throttles the large signal to a lower level to prevent ADC saturation.

TABLE III  
TYPES OF CSI DISTORTION

Type No.	Visual Form	Symmetry	Trigger Condition
Type I	M-shaped magnitude, horizontal S-shaped phase	Close to symmetrical	BW > 20 MHz, both Tx/Rx in HT20 or HT40 channel mode
Type II	inverted V-shaped magnitude, straight-line phase	Close to symmetrical	BW < 20 MHz, both Tx/Rx in HT20 or HT40 channel mode
Type III	Left or right half of Type I	Asymmetrical	One of Tx/Tx in HT20 mode, the other in HT40+/- mode

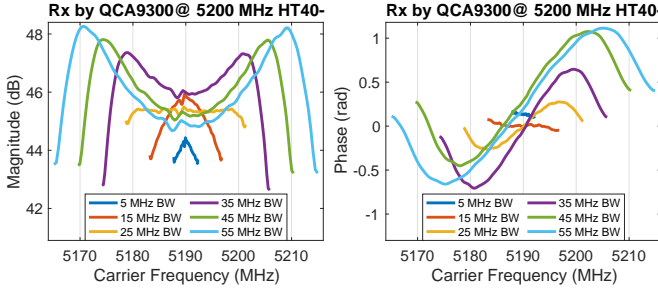


Fig. 10. CSI distortion (magnitude and phase response) under different bandwidths. Both Tx and Rx ends were QCA9300. They operated at 5200 MHz with HT20 channel mode and varying bandwidths.

5) *T5: Test of the influence of the bandwidth:* In this test, we used PicoScenes to scan the bandwidth of both QCA9300 NICs from 5 to 55 MHz in 5 MHz increments and, at each bandwidth, performed 1000 round-trip CSI measurements. To the best of our knowledge, this is *the first reported measurement of CSI at different bandwidths on COTS NICs*.

Fig. 10 shows the average magnitude and phase of the received CSI from Laptop A. The results are remarkable in that *the distortion clearly shows a bandwidth-related shape change*. More specifically,

- as the bandwidth increases, we observe an increase in the curvature of both the M-shaped magnitude distortion and the horizontal S-shaped phase distortion, and
- as the bandwidth decreases, the magnitude response deforms from an M shape to an inverted V shape, and the phase response deforms from a horizontal S shape to a roughly straight line.

*Summary of the test results:* Based on the above analysis, we draw the following conclusions:

- 1) There are three types of distortion, as listed in Table III.
- 2) Among the various influencing factors, the bandwidth is the dominant factor.
- 3) *Both* the Tx and Rx ends contribute to the distortion, although the Rx end contributes more.
- 4) The distortion is *pervasive* for all hardware, and in all channel configurations, the IWL5300 has stronger distortion than the QCA9300.
- 5) The Tx power and I/Q imbalance have essentially *no* influence on the distortion.

#### B. Reasonable conjectures regarding the cause of the distortion

Despite the lack of official documentation, we can make reasonable conjectures regarding the causes of the CSI distortion based on some widely accepted RF design principles.

The Type I distortion is highly likely to be a combined effect of the digital predistortion (DPD) module and the Rx-end ACR filter. The DPD module *intentionally* bends the Tx and Rx signals with an *inverse sinc* response to compensate, and possibly *overcompensate*, for the *sinc* fading caused by the Tx DAC. In regard to the CSI distortion, the overcompensation effect corresponds to the central inverted V-shaped part of the M-shaped magnitude distortion and the central straight-line part of the horizontal S-shaped phase distortion. It is worth noting that modest overcompensation is actually a desirable strategy for OFDM communication because it guarantees compensation for the fading caused by an unknown Tx end while having no meaningful impact on communication.

On the other hand, the rapid fading that occurs at both ends of the spectrum is clearly caused by the Rx-end ACR filter. The primary purpose of the ACR filter is to suppress the interference from adjacent channels. However, according to the principles of filter design, better rejection performance stands in conflict with smaller in-band distortion, given that the filter implementation in the NIC baseband is fixed and the order is low. As a result, NIC manufacturers often choose to trade in-band spectral flatness for better out-of-band rejection, which is reflected in the rapid fading at both ends of the spectrum. Regarding the QCA9300, the ACR filter is a fifth-order LPF, as previously discussed.

The Type II distortion may be due to a combination of weak DPD and Tx DAC fading. Type II distortion occurs only at a low bandwidth. In this case, according to the *scaling* property of Fourier transformation, the DAC *sinc* fading shrinks to a narrower spectrum around the direct current (DC). However, the DPD module, essentially a reconfigurable filter, is not associated with the baseband clocking<sup>2</sup> and therefore maintains its weak and flat response around the DC. This frequency mismatch produces an inverted V-shaped response.

The Type III distortion is actually either the left or right half of a Type I distortion. As mentioned above, when the HT40+/- mode channel communicates with the HT20 mode channel, only half of the bandwidth is utilized. Therefore, the half of the spectrum that is utilized corresponds to the left or right half of a Type I distortion. More specifically, when an HT20 channel communicates with an HT40+ channel, the CSI measured at both ends will be the left half of the M shape; when an HT20 channel communicates with an HT40- channel, the measured CSI will be the right half of the M shape.

#### C. CSI model revised for Wi-Fi sensing

According to tests T1, T2 and T5, the basebands on both the Tx and Rx ends cause distortion in the CSI. We use  $\mathbf{H}_{tx}$

<sup>2</sup>A technique for overriding the QCA9300's baseband filter and DPD module is still under study.

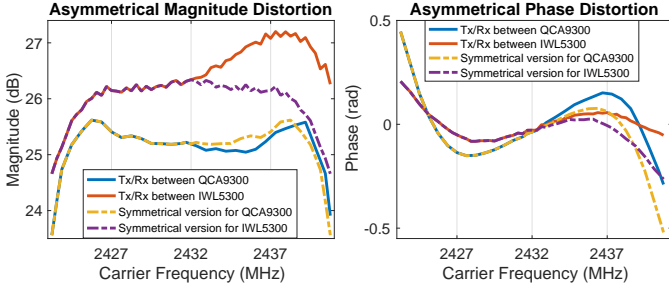


Fig. 11. Asymmetry property of the CSI distortion. The dashed lines on the right, which mirror the left parts of the curves, show significant differences from the actual measurements.

and  $\mathbf{H}_{rx}$  to denote their respective influences. Bringing them into (2), we arrive at the revised CSI model:

$$\mathbf{H}_{bb} = \mathbf{H}_{err} \cdot \mathbf{H}_{rx} \cdot \mathbf{H}_{air} \cdot \mathbf{H}_{tx} \quad (10)$$

Equation (10) explicitly accommodates the baseband distortion for the first time. However, (10) is difficult to apply in practice because it requires measuring  $\mathbf{H}_{tx}$  and  $\mathbf{H}_{rx}$  individually. Fortunately, in practical, we can merge these two distortions<sup>3</sup> and transform (10) into a simpler version as follows:

$$\begin{aligned} \mathbf{H}_{bb} &= \mathbf{H}_{dist} \cdot \mathbf{H}_{err} \cdot \mathbf{H}_{air} \\ \mathbf{H}_{dist} &= \mathbf{H}_{tx} \cdot \mathbf{H}_{rx} \end{aligned} \quad (11)$$

#### D. Why does the distortion contaminate Wi-Fi sensing but not Wi-Fi communication?

For OFDM communication, what matters is not the specific processes or filters the signal undergoes *but that all parts of the signal experience the exact same process*. Taking data symbols as an example, *i.e.*, the HT-Data symbols in 802.11n, the distortions in data symbols as well as other channel influences can be indifferently equalized by the training symbols (HT-LTF), which experience the same distortion. Unfortunately, in the Wi-Fi sensing context, this distortion is harmful, especially for phase-based sensing techniques relying on accurate in-air channel responses. The baseband distortion severely bends  $\mathbf{H}_{air}$  in a frequency-selective manner, thereby compromising performance in various accurate sensing applications.

In other words, **“channels” are interpreted differently in the contexts of OFDM communication and Wi-Fi sensing**. In the former context, a “channel” refers to the combined effect of all kinds of influences, including baseband distortion. However, in the context of Wi-Fi sensing, the popular interpretation of a “channel” refers to only one specific stage of the combined effect, *i.e.*, the in-air signal propagation.

#### E. How to get rid of the distortion

Previous works have proposed methods [14], [16], [11] of eliminating CSI distortion; however, they have all focused only on the phase distortion. Xie *et al.* [14] pruned the severely distorted subcarriers at both ends. Zhu *et al.* [16] and Tadayon *et*

<sup>3</sup>This is because  $\mathbf{H}_{tx}$  and  $\mathbf{H}_{rx}$  are both diagonal matrices, which allows the commutative law to be used on (10).

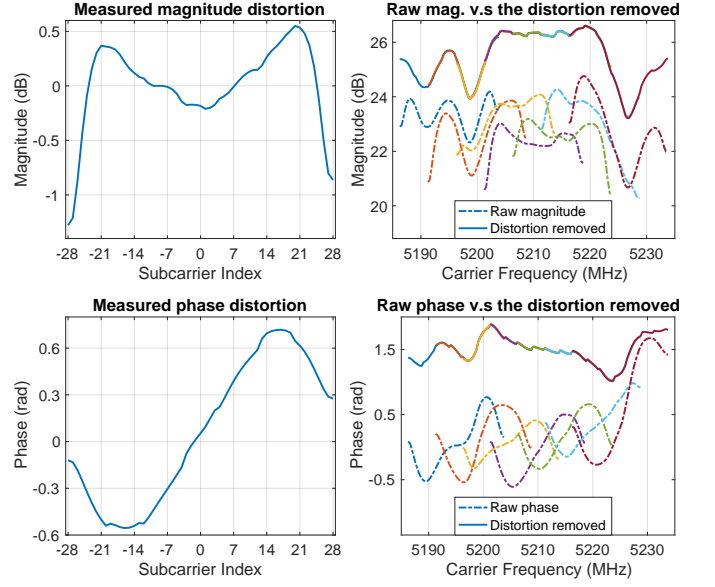


Fig. 12. Measured CSI distortion and the results of distortion removal. The left figures show the magnitude and phase distortion measured in a strong LoS situation. The figures on the right show both the magnitude and phase measurements before and after distortion removal. The severely distorted measurements become aligned and smooth after distortion removal.

*al.* [11] both attempted curve fit the phase distortion using a centrally symmetric function; however, the phase distortions in the HT40+/- channel modes are not symmetric, as shown in Fig. 1. Moreover, as shown in Fig. 11, neither the magnitude nor the phase is precisely symmetric in the HT20 mode.

We generalize the above methods by storing the raw distortion rather than curve fitting or pruning the distortion. As a result, we achieve a general distortion removal method that covers both the magnitude and phase distortions. Quite similar to the prior approaches, the user first explicitly measures the CSI distortion between all Tx and Rx pairs before the deployment of a sensing application. This measurement can be done by connecting the Tx and Rx with cables or placing them in a very strong line-of-sight (LoS) situation. For each Tx/Rx pair, the CSI is measured, and the average magnitude and phase distortions are stored. Then, in the sensing stage, for each CSI measurement, the stored distortions in the magnitude and phase domains are subtracted, and then, the complex-valued CSI is reconstructed.

The next problem is how to verify the correctness of the distortion removal. Zhu *et al.* [16] stitched together adjacent CSI measurements based on the insight that *the CSI measurements from adjacent yet partially overlapping channels should have identical measurements in the shared part*. We adopt the same idea to verify the correctness of the distortion removal. Fig. 12 shows an example of distortion removal. The disjoint raw measurements from adjacent channels become smooth and aligned with each other after distortion removal.

However, we should note that the stitched phase results cannot reflect the propagation distance. This is due to the existence of the STO, SFO and SCO as well as OFDM pre-advancement [11]. Their nonzero means contaminate the overall slope of the stitched phase. We are working on a

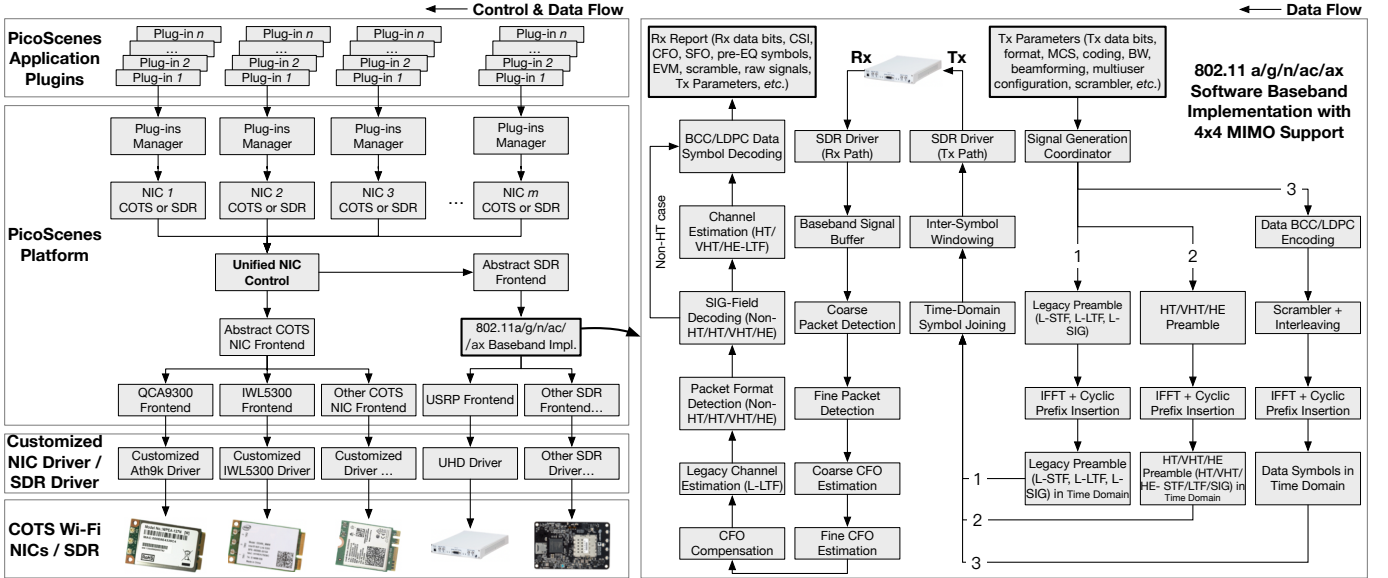


Fig. 13. Software architecture of the PicoScenes system. PicoScenes consists of 3 layers, namely, the PicoScenes drivers, the PicoScenes platform and the PicoScenes plugin subsystem. The drivers provide access to various hardware features. The platform abstracts the features into powerful APIs. The plugins perform the core measurement tasks. To support SDR-based Wi-Fi sensing, PicoScenes includes an embedded software baseband implementation, as shown on the right.

solution to recover the overall slope. However, this is ongoing research and is beyond the scope of this paper.

## V. PICOSENES PLATFORM

We introduce PicoScenes, a powerful, hardware-unified and extensible Wi-Fi sensing platform that is designed to meet the most challenging requirements of modern Wi-Fi sensing research. In the following text, we present the architecture of PicoScenes and some design highlights.

### A. PicoScenes Architecture

PicoScenes consists of 3 layers from bottom to top, as shown on the left of Fig. 13, namely, the PicoScenes drivers, the PicoScenes platform and the PicoScenes plugin subsystem.

**PicoScenes Drivers:** We created our own versions of kernel drivers for both the QCA9300 and the IWL5300. These drivers extract the CSI and expose various hardware controls directly to the user space. We have improved upon the original drivers in three main respects: First, we have added a multi-NIC concurrent CSI measurement functionality by refactoring the CSI data collection onto a per-device data structure, which allows the PicoScenes software to access the CSI from multiple NICs concurrently. Second, we provide a unified data format across the QCA9300, the IWL5300 and even SDR devices. All of the data components, the Rx descriptor, the CSI, the packet content and extra Tx/Rx information are self-descriptive and versioned *segments*. All segments can be decoded only by version-matched parsers. In this way, we achieve forward compatibility for future upgrades. Third, we have significantly simplified the installation of the PicoScenes drivers. Instead of the cumbersome building of an old kernel on an obsolete OS, the PicoScenes drivers are released directly in the form of a prebuilt Debian .deb package of less than 1 MB in size. It

depends on the latest OS and the latest kernel version. Users can install it by simply double-clicking.

**PicoScenes Platform:** The PicoScenes platform is essentially the middleware for Wi-Fi sensing. In addition to basic CSI data collection, it integrates packet-injection-based Tx control. It also abstracts the details of all types of frontend devices and exposes unified, powerful and user-friendly APIs to the measurement-specific plugin layer. The platform is extensible so that new CSI-extractable hardware can be easily accommodated by adding descriptive frontend instances.

The PicoScenes platform is itself a layered architecture. At the bottom is the frontend. For each supported NIC and SDR device, we have a Frontend class that encapsulates all supported controls. Thanks to our detailed study of the QCA9300 hardware, PicoScenes is greatly advantageous for the QCA9300. In addition to the aforementioned arbitrary tuning of the carrier frequency and bandwidth, PicoScenes enables other valuable features for the QCA9300, such as selecting the Tx/Rx radio chain, transmitting extra spatial sounding (ESS) version packets and accessing the hardware registers. On top of the frontend, there is an abstraction layer that exports the unified APIs to the upper-level plugins. To support the SDR-based frontend, we have developed and embedded a high-performance Wi-Fi baseband processing implementation under the Abstract SDR Frontend class, which can drive the SDR hardware to function like a full-featured Wi-Fi NIC. We call this mode PicoScenes on SDR, and we describe it in detail later. Above the abstraction layer, each NIC abstraction has a plugin manager that finds, installs and controls the lifetime cycle for plugins at run time.

Performance is also a core concern. The whole platform, written in C++20, embraces a multithread design from the ground up. All performance-sensitive tasks, such as the frontend I/O, baseband decoding/encoding for SDR, NIC-level

TABLE IV  
AN INCOMPLETE LIST OF FEATURES FOR COMPARISON BETWEEN PICOSENES AND EXISTING CSI EXTRACTION TOOLS

Feature	CSI Measurement/Extraction Tools			
	PicoScenes	Intel 5300 CSI Tool [13]	Atheros CSI Tool [14]	Nexmon CSI Extractor [15]
Supported frontend	IWL5300, QCA9300, USRP and <i>more</i>	IWL5300	QCA9300	BCM43xx
>10 kHz packet injection & CSI measurement	✓ for all			✗
Concurrent multi-NIC CSI extraction	✓ for all		✗	
In situ CSI parsing & processing	✓ for all		✗	
CSI measurement for QCA9300→IWL5300	✓ for all		✗	
Turning on/off selected radio chain(s)	✓ for all		✗	
Unified, open and self-descriptive CSI data format	✓ for all		✗	
Support for secondary development	✓ for all		✗	
Arbitrary bandwidth and carrier frequency tuning	✓ for QCA9300 and SDR		✗	
Transmission of extra sounding HT-LTF	✓ for QCA9300 and SDR		✗	
Access to Rx EVM	✓ for QCA9300 and SDR		✗	
CSI measurement for all MAC addresses	✓ for SDR		✗	
VHT/HE-rate packet injection	✓ for SDR		✗	
Tx/Rx with 4x4 MU-MIMO/OFDMA/beamforming	✓ for SDR		✗	
Reporting of CSI for 11ax packets	✓ for SDR		✗	
Easy installation without kernel build	✓ “apt install” + auto-update		✗	
Round-trip measurement with channel scan	✓ (by EchoProbe plugin)		✗	
Support for latest kernel versions	✓ currently on v5.4 LTS	✗		✓ v5.4 LTS
Works on latest host OSs	✓ Ubuntu 20.04 LTS		✗	✓ 18.04 LTS

jobs and all plugin instances, run in separate threads. In this way, measurement jobs specific to multiple NICs can be performed concurrently without congestion.

*PicoScenes Plugin Subsystem:* This subsystem performs application- and measurement-specific tasks. The plugins invoke the hardware-independent APIs exposed by the platform to implement various Wi-Fi sensing or communication tasks in a task-centric manner. We have made the PicoScenes plugin development kit (PSPDK) open source, which enables users to develop their own measurement plugins.

As a demonstration of the PSPDK, we have developed EchoProbe, a PSPDK-based plugin that can orchestrate two PicoScenes nodes to perform round-trip CSI measurement and spectrum scanning through packet-injection-based communication. There are two roles defined by EchoProbe: an initiator and a responder. The initiator injects the self-defined `CSIProbeRequest` frame, and the responder then receives the frame and packages the measured CSI as the reply payload to be sent back to the initiator. In this way, EchoProbe measures the round-trip CSI in <1 ms. Furthermore, it features a *synchronized jump* that tunes  $f_c$  and  $f_{bb}$  for both nodes at the same time. In this way, EchoProbe achieves round-trip CSI measurement over a wide spectrum.

*PicoScenes CLI:* PicoScenes provides a powerful and user-friendly command line interface (CLI). For example, the following commands specify two NICs, #1 on laptop A and #2 on laptop B, to perform spectral scanning of both carrier frequency and bandwidth:

```
PicoScenes -i 1 -mode responder (run on laptop A)
PicoScenes -i 2 -mode initiator -cf 2.3e9:5e6:2.4e9 -sf
  20e6:5e6:60e6 -repeat 200 -delay 1e3 -mcs 2 -ess
  1 -txcm 4 -rxcm 7 (run on laptop B)
```

where NIC #1, on laptop A, works in the EchoProbe *responder* mode (-i 1 -mode responder), whereas NIC #2, on laptop B, is the round-trip measurement *initiator* (-i 2 -mode initiator).

TABLE V  
EXTRA PHY-LAYER INFORMATION PROVIDED BY PICOSENES ON SDR

Feature Name	Data Type
HT/VHT-SU/HE-SU CSI	complex double array
VHT-MU/HE-MU per-user CSI	complex double array
Legacy CSI (based on L-LTF)	complex double array
Raw baseband signal	complex double array
Pre-equalized OFDM symbols	complex double array
Phase diffs of pilot subcarriers	double array
CFO estimation (based on L-LTF)	double
Rx EVM	double
Noise floor	double
Timestamp (by hardware baseband clock)	double
Scrambler initial value	8-bit integer

The initiator scans both the carrier frequency from 2300 to 2400 MHz in 5 MHz increments (`-cf 2.3e9:5e6:2.4e9`) and the bandwidth from 20 to 60 MHz in 5 MHz increments (`-sf 20e6:5e6:60e6`). For each rate combination, NIC #2 performs 200 round-trip measurements at 1000  $\mu$ s intervals (`-repeat 200 -delay 1e3`). Each packet is transmitted with MCS index 2 and with 1 ESS HT-LTF (`-mcs 2 -ess 1`). Finally, the command further specifies the Tx/Rx radio chains of NIC #1: the Tx uses the third radio chain, and the Rx uses all three radio chains (`-txcm 4 -rxcm 7`).

Table IV lists the major advantages of the PicoScenes system over existing CSI tools.

#### B. PicoScenes on SDR

Despite its increasing popularity, the adoption of SDR in Wi-Fi sensing is severely hampered by a lack of baseband signal processing functionality. As illustrated on the right side of Fig. 13, we have addressed this issue by developing and embedding an 802.11a/g/n/ac/ax-compatible baseband imple-

mentation into the PicoScenes platform, thereby transparently empowering SDR devices to function like full-featured Wi-Fi NICs. We call this feature PicoScenes on SDR<sup>4</sup>, and it currently supports two hardware models, the USRP N210 and X310 models. With PicoScenes on SDR, the adoption of SDR in Wi-Fi sensing is *unprecedentedly simplified*. Taking the PicoScenes commands above as an example, replacing “-i 2” with “-i usrp192.168.10.2” is all that needs to be done to switch to the USRP with IP address 192.168.10.2. The substitute USRP-based EchoProbe initiator will perform exactly the same measurement process, except that it will return much richer measurement results.

One of the most attractive aspects of PicoScenes on SDR is that it provides *complete* control over the Wi-Fi Tx and Rx, which has overwhelming advantages for Wi-Fi sensing applications and research based on COTS NICs. On the Tx side, the user can specify the initial scrambler value, which is crucial for Wi-Fi-based cross-technology communication (CTC); beamforming, which enables fine-grained sensing and calibration; and ESS, which enables a COTS NIC to measure additional CSI for a single 802.11n frame. On the Rx side, as listed in Table V, PicoScenes returns the complete PHY-layer information. We believe that this unprecedented PHY-layer information can enable more diverse and more accurate sensing applications, such as precise CFO/SFO/STO/SCO estimation, accurate ToF estimation and distributed phased arrays. In addition, the unified interface for Wi-Fi communication (from 802.11a to 802.11ax multiuser (MU) profiles) and high spectrum and bandwidth accessibility simplify the prototyping and development of new Wi-Fi communication and sensing applications.

### C. PicoScenes MATLAB Toolbox

PicoScenes adopts a *variable and extensible CSI structure* such that the CSI data measured from different NIC models and even SDR devices share the same entity structure. Furthermore, PicoScenes and the MATLAB Toolbox share a single CSI/baseband data parsing routine, which guarantees consistency between C++-based and MATLAB-based data parsing and manipulation. In addition to data parsing, the Toolbox ships with many convenient features, such as one-step installation, .csi file drag-and-drop parsing and a MATLAB App named “.csi File Batch Loader”.

### D. Software Release

PicoScenes is released at <https://zpj.io/ps><sup>5</sup>.

## VI. EVALUATION OF THE PICOSENES PLATFORM

In this section, we report extensive evaluations of the functionality and performance of the PicoScenes system. We divide the evaluations into two subsections based on the hardware used: PicoScenes on COTS Wi-Fi NICs and PicoScenes on SDR. Finally, we briefly summarize the evaluations.

<sup>4</sup>PicoScenes on SDR contains proprietary code provided by an upstream vendor under an NDA; therefore we do not discuss its design details here.

<sup>5</sup>The PicoScenes software has already been released. The installation guide is also complete. During the review process, we are preparing a long and complete software manual.

---

### Listing 1 QCA9300 full-spectrum evaluation procedure

---

```

1:  $F_C = \{2.2 \sim 2.9, 4.4 \sim 6.1\}$  GHz with 20 MHz intervals
2:  $F_{BB} = \{2.5, 5, 10, 20, 30, 40, 50, 60\}$  MHz, 30 MHz and
   below with HT20, 40 MHz and above with HT40+
3:  $N_{STS} = \{1, 2, 3\}$ ,  $MCS = \{0, 4\}$ 
4: for each  $f_c \in F_C$  do
5:   for each  $f_{bb} \in F_{BB}$  do
6:     for each  $n_{sts} \in N_{STS}$  do
7:       for each  $mcs \in MCS$  do
8:         Perform 5000 round-trip CSI measurements
9:         and log the success rate.
10:      end for
11:    end for
12:  end for
13: end for

```

---

### A. Evaluation of PicoScenes on COTS Wi-Fi NICs

In this section, we evaluate the three most advantageous features of PicoScenes: spectrum and bandwidth tuning on the QCA9300, multi-NIC CSI measurement, and  $>10$  kHz packet injection and CSI measurement.

1) *Evaluation of the channel availability of spectrum and bandwidth tuning on the QCA9300*: Sections III-B2 and III-B3 describe how we achieve arbitrary tuning of both the baseband bandwidth  $f_{bb}$  and the carrier frequency  $f_{rf}$  for the QCA9300. However, some questions arise: *Are the newly available frequencies practically feasible? How good is the link quality at these frequencies?*

To answer this question, we conducted a comprehensive link quality evaluation covering the entire available spectrum and bandwidth. In the evaluation, two ThinkPad X201 laptops were placed 3 m apart in a small room without interference. Both laptops were equipped with QCA9300 NICs and were running Linux Mint 20 (a variant of Ubuntu 20.04 LTS) with kernel version 5.4.65. We enumerated a total of 5856 different channel configurations (122 carrier frequencies, 8 bandwidths, 3 spatial-time stream ( $N_{STS}$ )<sup>6</sup> values, and 2 MCS indices), as detailed in Listing 1. In each configuration, we used PicoScenes (with the EchoProbe plugin) to perform 5000 round-trip CSI measurements between the two laptops and logged their success rates. We define the success rate as the ratio between the target number of 5000 and the number of actual round-trip measurement trials. Fig. 14 shows the stacked success rates in the evaluation.

From Fig. 14, especially (A) to (C), we can see that the QCA9300 exhibits a high level of link quality consistency across the entire 2.4 GHz wide spectrum (2.2-2.9 GHz and 4.4-6.1 GHz). In other words, we do not see differences between the standard Wi-Fi channels and the channels made available by PicoScenes, even if the latter lack dedicated RF calibration. From (B) to (E), we see that a bandwidth of 50 MHz and above seems to yield better performance in the 2.4 GHz band than in the 5 GHz band. This may be because the RF synthesizer

<sup>6</sup>The definition of the MCS index is narrowed in 802.11ac/ax protocols, where  $N_{STS}$  is decoupled from the MCS index. For consistency of description, we use the 802.11ac/ax-based definition of the MCS index throughout the evaluations.

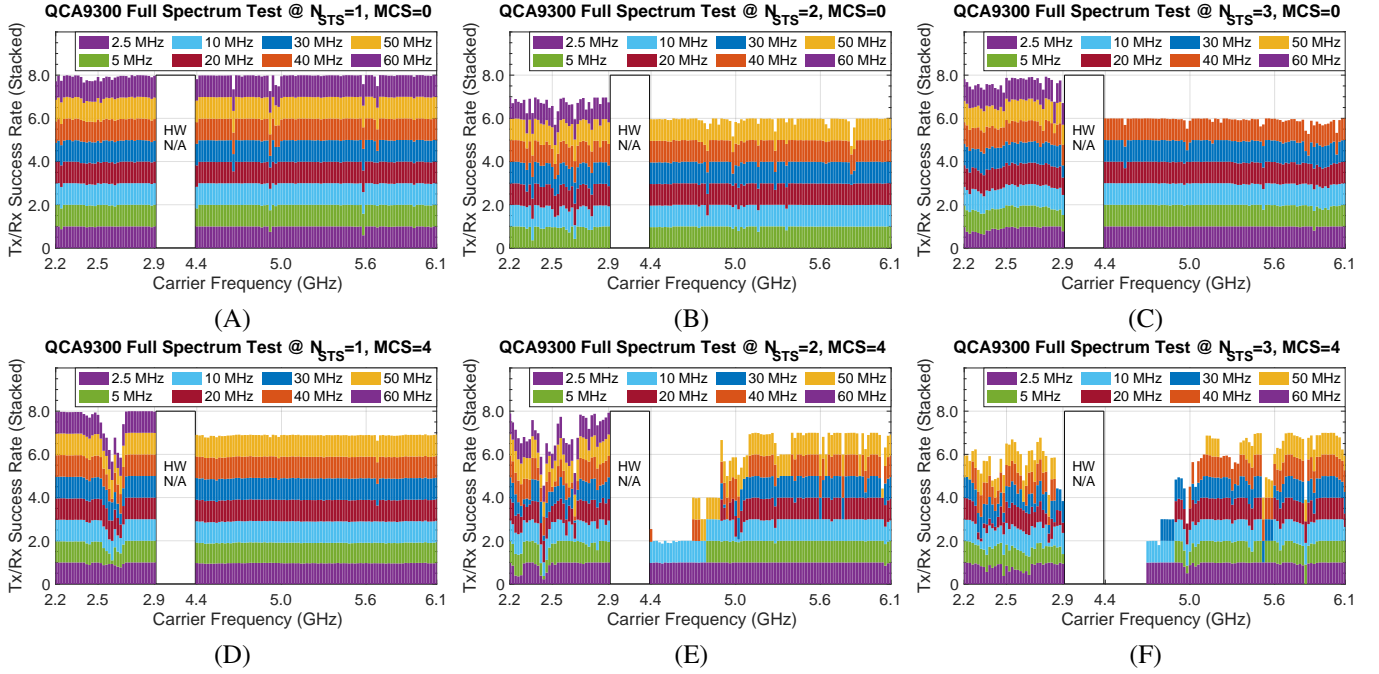


Fig. 14. Stacked Rx success rates in a full-spectrum and full-bandwidth link quality evaluation on the QCA9300. The evaluation covers 5856 configurations.

provides a higher adjustment accuracy in the 2.4 GHz band. (E) and (F) show a large drop in link quality at approximately 4.4-4.9 GHz; compared to (B) and (C), their only difference is the increase in the MCS index from 0 to 4. This comparison indicates that the RF synthesizer seems to have higher error in the 4.4-4.9 GHz spectrum. To improve the performance in this short spectrum, we will need to recalibrate the device; the related reverse engineering process is still under investigation.

From the perspective of bandwidth availability, the QCA9300 shows good link quality at bandwidths of 40 MHz and below. The sub-20 MHz bandwidth shows superior link resilience in all test cases, even in MCS=4 cases. This is because the lower baseband bandwidth improves the clocking error tolerance. If we focus on the 2.4 GHz band, the QCA9300 still performs quite well in the above-standard 30/40/50/60 MHz bandwidth cases. Taking the MCS=0 cases as an example, the performance at a 60 MHz bandwidth, 1.5x the standard bandwidth, shows good link quality, even with 3 spatial streams. The practical availability of higher bandwidths is quite useful in Wi-Fi sensing, as such bandwidths provide higher temporal resolution as well as a shorter transmission time. We also tried to expand the evaluation to 70 MHz and even 80 MHz bandwidths. Unfortunately, at such high bandwidths, the excessive number of transmission failures led to early termination of the evaluation.

2) *Evaluation of concurrent CSI measurement for multiple COTS Wi-Fi NICs:* Multi-NIC concurrent CSI measurement is one of the most advantageous features of PicoScenes. In this section, we present a reference design for a multi-NIC Wi-Fi sensing array, which contains 27 NICs in our case. We then evaluate its concurrent CSI measurement performance.

Fig. 15 shows a photograph and the layout of our modular-designed 27-NIC sensing array. Its core architecture is a 3-

layer PCI-E hierarchy in which the branch nodes are PCI-E 1-to-3 bridge adapters and the leaf nodes are QCA9300 NICs. For the power supply, we use multiple power-splitting cords to distribute electricity to the bridge adapters and the NICs. For the data connections, PCI-E extension cords (actually USB 3.0 cables) are used to connect the bridge adapters and the host PC. The array is encapsulated in an IKEA box, which exposes only two external connections. The total bill of materials (BOM) for the array is less than 700 USD, *i.e.*, merely 8.6 USD per radio chain. To the best of our knowledge, this is the largest and probably the most cost-efficient multipurpose Wi-Fi sensing array built on the basis of COTS NICs.

To evaluate the performance of the array, we attached the 27-NIC array and another QCA9300 NIC to a desktop computer. An additional QCA9300 NIC was used for packet injection. The computer was equipped with an i9-10850K CPU, 32 GB of RAM, 512 GB of SSD, and a 750 W power supply. We evaluated the performance of concurrent CSI measurements with different numbers of Rx NICs ( $N_{NIC} \in \{9, 18, 27\}$ ), bandwidths ( $BW \in \{20, 40\}$  MHz) and Tx injection speeds. In each test case, we used PicoScenes to inject 100k packets and log the Rx success rate (Rx rate hereafter). We define the Rx rate as the ratio between the number of actually received frames and the total number of injected frames. The injected packets were 32 B data frames (including a 4 B frame check sequence) that we used as the CSI probes. By modulating these frames with  $MCS \geq 4$ ,  $N_{STS} = 1$  and a 400 ns guard interval, each frame was encoded to only 864 baseband samples, which is also the shortest 802.11n frame for which both the QCA9300 and IWL5300 can measure CSI. When transmitted at a 20 MHz bandwidth, the duration of this frame is 43.2  $\mu$ s. The reason for transmitting this carefully designed frame was to maximize the speed of CSI measurement; accordingly, we

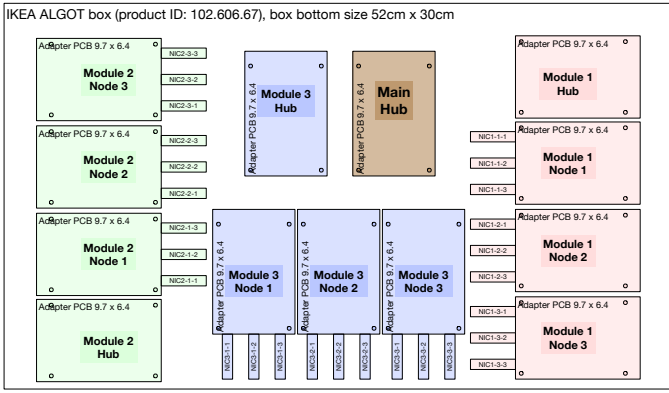
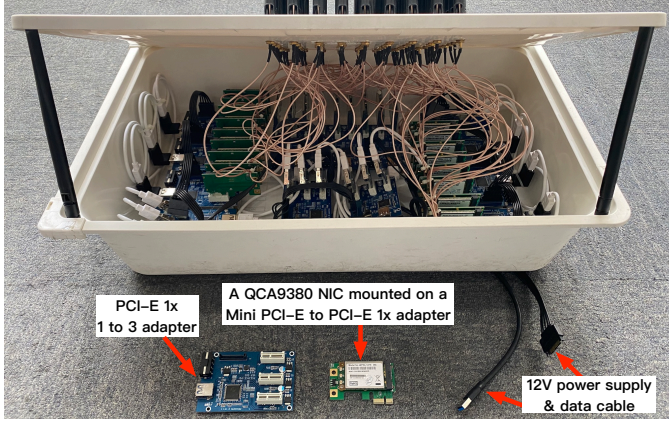


Fig. 15. Photograph and design layout of a 27-NIC Wi-Fi sensing array. The 27-NIC array consists of 3 “modules” and a “main hub”. Each module contains 4 PCI-E 1x 1-to-3 bridge adapters and 9 QCA9300 Wi-Fi NICs. The array is contained in an IKEA box.

call this frame the “CSI Probing Frame” hereafter.

Fig. 16 shows the impressive results. In the 20 MHz bandwidth cases, the array achieves a >97% mean Rx rate when  $N_{NIC} \leq 18$  and still has a >91% Rx rate when  $N_{NIC} = 27$ . Moreover, in all 20 MHz bandwidth cases, an increase in the injection rate seems to have a negligible impact on the Rx rate. The two results above clearly prove the high efficiency of the concurrent architecture of PicoScenes. In fact, PicoScenes schedules more than 120 threads to support the concurrent operation of 27 NICs.

To explore the performance limits, we boosted the standard 20 MHz bandwidth to 40 MHz. At a 40 MHz bandwidth, an approximately 7% decline in the Rx rate is observed in the  $N_{NIC} = 9$  and  $N_{NIC} = 18$  cases. This is due to the low tolerance to clocking error associated with the high bandwidth. The expected performance drop occurs in the  $N_{NIC} = 27$  case. In this extreme case, the kernel driver seems to become the performance bottleneck. The reason is that, because the QCA9300 is a soft-MAC NIC, the reception of every single Wi-Fi frame requires the host CPU to execute thousands to tens of thousands of instructions. However, the ath9k kernel driver is not architecturally optimized for our multi-NIC and multi-bandwidth communication scenario. Therefore, the driver dispatches the massive number of kernel jobs to only a few specific or even a single CPU core(s). This leads to a greatly biased CPU load in the kernel space, and consequently,

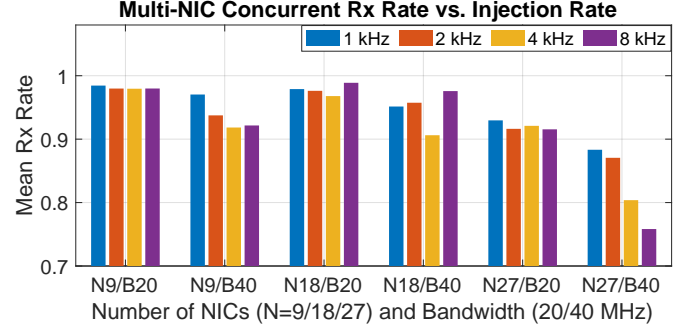


Fig. 16. Rx success rates of multi-NIC concurrent CSI measurements given different numbers of NICs, bandwidths and Tx injection rates. The Y-axis represents the *mean* Rx rate in multiple tests.

the Rx performance drops. In the 40 MHz bandwidth case, the doubled instantaneous traffic intensifies this problem.

Before ending the discussion of the multi-NIC evaluation, we answer two important questions.

*Is this a phased array?* No. In the current setup, all 27 NICs are time independent and therefore unsynchronized. The existing approach for implementing a phased 27-NIC array is Phaser [21]; however, it requires sacrificing 1/3 of the antennas to perform cross-NIC time synchronization. We are working on an optimized solution based on the current 27-NIC array; however, it is beyond the scope of this paper.

*Can we build an IWL5300-based multi-NIC sensing array?* Yes, of course. The kernel driver enhancement for concurrent CSI measurement is actually *shared* between the QCA9300 and IWL5300 models. In addition to the driver, in the PicoScenes software, the support for concurrent CSI measurement is also invariant for the QCA9300, the IWL5300 or any other supported hardware.

3) *Evaluation of the maximum packet injection rate and CSI measurement speed:* Another promising feature of PicoScenes is >10 kHz packet injection and CSI measurement. We conducted a thorough evaluation to answer two simple questions:

*How quickly can these devices inject packets?*

*How quickly can these devices measure the CSI?*

In this evaluation, for each device and all its supported bandwidths, we used PicoScenes to inject 200k CSI Probing Frames as quickly as possible. The evaluation encompassed QCA9300, IWL5300, and SDR devices. SDR is a special case for which we provide two working modes: a real-time mode and a replay mode. Both modes are based on PicoScenes on SDR. In the former, the baseband signals are generated and transmitted immediately, while in the latter, the *baseband signals are generated, saved to a file, and then replayed in a second run*. In this way, by controlling the length of the interframe spacing (IFS), the replay mode can drive an SDR device to reach the theoretical limit of packet injection.

Fig. 17 shows the results. The QCA9300 NIC yields a rate of 10845 Hz, *i.e.*, 92  $\mu$ s per packet on average. The IWL5300 yields only a 6350 Hz maximal injection rate, *i.e.*, 157  $\mu$ s per packet on average. For SDR in real-time mode, PicoScenes yields 4304 Hz on the USRP X310, *i.e.*, 232  $\mu$ s per packet on average. In regard to the software-based

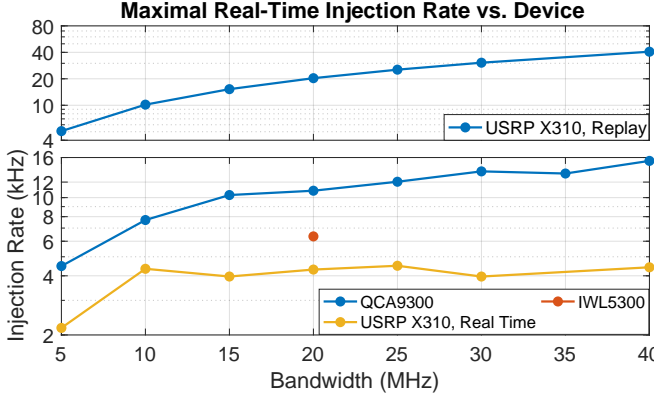


Fig. 17. Maximal packet injection rate by device.

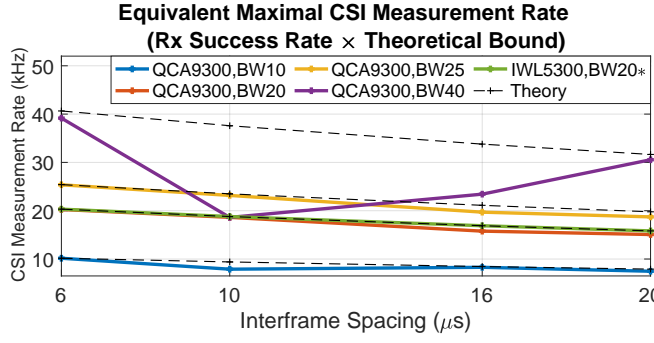


Fig. 18. Maximum CSI measurement rate by device.

baseband encoding, we believe this is a very good result. The injection rates achieved in replay mode are identical to the theoretical limit. Taking a 20 MHz bandwidth as an example, the theoretical limit of the injection rate is calculated to be  $20M/(864+120) = 20325$ , where the 120 samples correspond to the 6  $\mu\text{s}$  IFS for the 20 MHz bandwidth.

To answer the second question regarding the maximal CSI measurement rate, we conducted another straightforward evaluation. We used the replay mode of PicoScenes on SDR to pregenerate and replay 50000 CSI Probing Frames at the theoretical limit rate and logged the Rx rate. Then, we multiplied the Rx rate by the theoretical limit to obtain the equivalent maximal CSI measurement rate.

Fig. 18 shows the results. The most impressive result is that the QCA9300 attains a 40 kHz CSI measurement rate under a 40 MHz bandwidth and the shortest IFS of 6  $\mu\text{s}$ . Regarding the maximal 40 kHz rate, it is not surprising that the QCA9300 reaches very close to the theoretical limit at lower bandwidths and larger IFS values. For the IWL5300, we see that its Rx performance is also very close to the theoretical limit; however, during the evaluation, we experienced *extremely frequent* firmware crashes shortly after the start of the signal burst. We omit the test of the real-time mode of PicoScenes on SDR in this section, as it will be covered later.

### B. Performance evaluation of PicoScenes on SDR

We evaluated the performance of PicoScenes on SDR in two stages. In the first stage, we utilized the internal loopback

### Listing 2 Performance evaluation for PicoScenes on SDR

```

1:  $FMT = \{11a/g, 11n, 11ac-SU, 11ax-SU\}$ 
2:  $CBW = \{20, 40, 80, 160\}$  MHz
3:  $N_{STS} = \{1, 2, 3, 4\}$ 
4:  $MCS = \{0 - 7\}$ 
5:  $CODING = \{\text{BCC, LDPC}\}$ 
6:  $LEN = \{250, 500, 1000, 2000, 4000, 8000\}$  MHz
7: for each  $fmt \in FMT$  do
8:   for each  $cbw \in CBW$  do
9:     for each  $n_{sts} \in N_{STS}$  do
10:    for each  $mcs \in MCS$  do
11:      for each  $code \in CODING$  do
12:        for each  $len \in LEN$  do
13:          if  $is\_valid(fmt, cbw, n_{sts}, mcs, code, len)$  then
14:            Repeat the encoding  $\rightarrow$  decoding loopback
15:            for 1000 times, and log the time consumption.
16:          end if
17:        end for
18:      end for
19:    end for
20:  end for
21: end for
22: end for

```

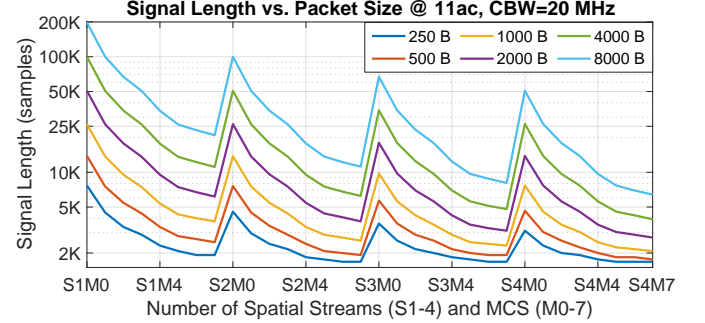


Fig. 19. Baseband signal length under different packet lengths,  $N_{STS}$  and MCSs. The measurement was performed with the 802.11ac protocol and 20 MHz CBW.

mechanism of PicoScenes to comprehensively measure the encoding and decoding performance for the Wi-Fi baseband signal *w.r.t.* the protocol, channel bandwidth (CBW)<sup>7</sup>,  $N_{STS}$ , MCS, coding scheme and packet length. In the second stage, we introduced PicoScenes into real-world CSI measurement scenarios and measured its real-time performance *w.r.t.* the injection rate,  $N_{STS}$  and number of Rx antennas ( $N_{Ant}$ ).

1) *Stage 1: Performance evaluation of PicoScenes on SDR via loopback:* In this evaluation, we looped back the encoded Wi-Fi baseband signal directly into the decoder; in this manner, we obtained interference-free performance measurements for both the encoder and decoder. As shown in Listing 2,

<sup>7</sup>The CBW refers to the parameter of the bandwidth used in encoding. In this paper, the CBW is not necessarily equal to the baseband bandwidth. For example, as shown in Fig. 14, we transmit 802.11n HT20 (CBW=20 MHz) and HT40+/- (CBW=40 MHz) packets with multiple different bandwidths.

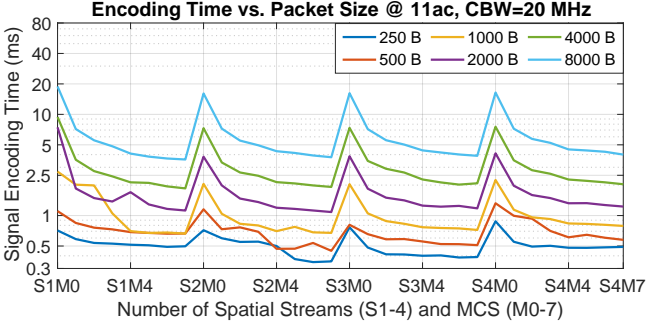


Fig. 20. Baseband signal encoding times under different packet lengths and different  $N_{STS}$  and MCS settings. The measurements were performed with the 802.11ac protocol and a 20 MHz CBW.

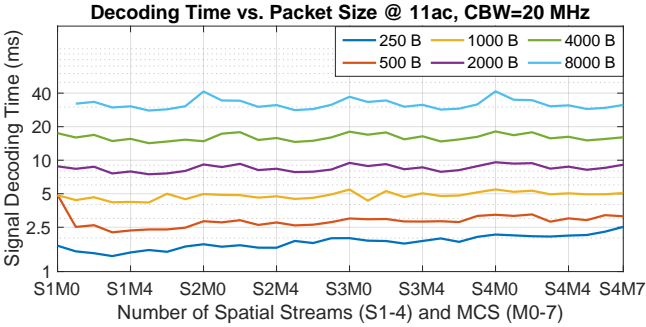


Fig. 21. Baseband signal decoding times under different packet lengths and different  $N_{STS}$  and MCS settings. The measurements were performed with the 802.11ac protocol and a 20 MHz CBW.

we enumerated  $>3000$  valid channel configurations in total<sup>8</sup>. In each configuration, we encoded/decoded 1000 packets and measured the encoding time, decoding time and signal length. The computer used for the evaluation was equipped with an i9-10850K CPU, 32 GB of RAM, and 512 GB of SSD. The results are shown in Figs. 19 to 25.

Fig. 19 presents the length of the encoded signal (in samples) *w.r.t.* different packet lengths (in bytes) and different  $N_{STS}$  and MCS settings. This figure shows that an increase in both the  $N_{STS}$  and MCS values can dramatically reduce the signal length, with a change in the MCS index leading to a greater signal length reduction than a change in  $N_{STS}$ . We chose the 802.11ac protocol with a 20 MHz CBW and BCC as the baseline protocol rather than the 802.11n protocol. This is because, compared to 802.11n or the latest 802.11ax protocol, 802.11ac is more inclusive in its baseband configuration. It supports a CBW of up to 160 MHz and both BCC and LDPC coding in single-user (SU) or multiuser (MU) scenarios. This inclusiveness allows us to compare the performance across different CBWs, protocols and coding schemes.

Figs. 20 and 21 present the encoding and decoding times, respectively, *w.r.t.* the packet length.

These two figures reveal four interesting aspects of PicoScenes on SDR. First, the signal length and the correspond-

<sup>8</sup>Some of the configurations are invalid, such as a  $>20$  MHz CBW for the 11a/g protocol, a  $>40$  MHz CBW for the 11n protocol, BCC coding for a  $>40$  MHz CBW in the 11ax protocol, and some special cases, such as the invalid configuration of  $N_{STS}=3$  and MCS=6 for the 11ac protocol.

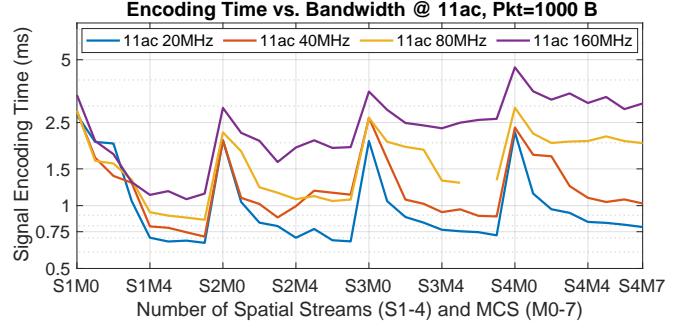


Fig. 22. Baseband signal encoding times under different CBWs and different  $N_{STS}$  and MCS settings. In each configuration, the packet to be encoded was a 1000 B single-user packet.

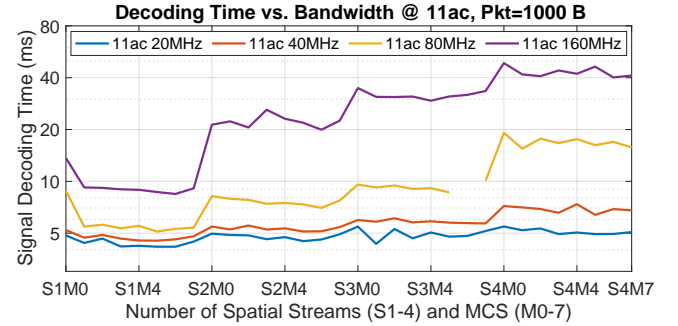


Fig. 23. Baseband signal decoding times under different CBWs and different  $N_{STS}$  and MCS settings. In each configuration, the baseband signal to be decoded was previously encoded from a 1000 B single-user packet.

ing encoding time show very similar trends. This is because the  $N_{STS}$  and MCS settings control the encoded length of a packet (in bits) and the time that the BCC encoder consumes is linear in the encoded length. Second, the decoding time, in contrast, seems completely independent of the signal length but strongly proportional to the packet length. This is because the time consumed by the BCC decoder, in contrast to that consumed by the encoder, is proportional to the raw packet length (in bytes) regardless of the encoded length. Third, we observe that the decoding time consumption is roughly double the maximal encoding time. This can be attributed to the nature of the forward error correction (FEC) in the BCC codec; that is, as a forward error coding scheme, its decoder consumes more time than the encoder. Finally, in terms of the specific time consumption, PicoScenes on SDR provides encoding performance at the  $<1$  ms level and decoding performance at the  $<2$  ms level for 250 B packets, which is equivalent to approximately  $>1000$  Hz packet encoding and  $>500$  Hz packet decoding. We believe that such high performance accompanied by the availability of rich PHY-layer information will be very attractive for Wi-Fi sensing research.

Figs. 22 and 23 present the encoding and decoding times, respectively, *w.r.t.* the CBW.

In contrast to Figs. 20 and 21, if we look carefully, Figs. 22 and 23 show not only an average time increase but also a stair-step time increase in both the encoding and decoding times. The configurations that trigger the stair-step increase

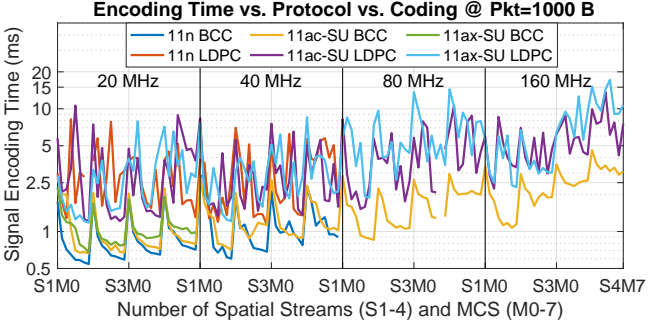


Fig. 24. Baseband signal encoding times under different protocols, CBWs, and  $N_{STS}$  and MCS settings. In each configuration, the packet to be encoded was a 1000 B single-user packet.

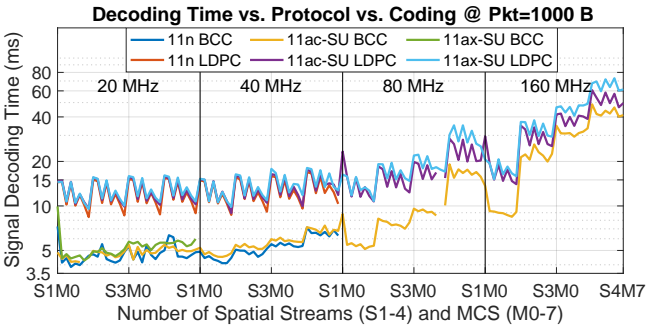


Fig. 25. Baseband signal decoding times under different protocols, CBWs, and  $N_{STS}$  and MCS settings. In each configuration, the baseband signal to be decoded was previously encoded from a 1000 B single-user packet.

are (CBW=40 MHz,  $N_{STS} = 4$ , MCS = 0), (CBW=80 MHz,  $N_{STS} = 2$ , MCS = 0), (CBW=80 MHz,  $N_{STS} = 4$ , MCS = 0), (CBW=160 MHz,  $N_{STS} = 2$ , MCS = 0), (CBW=160 MHz,  $N_{STS} = 3$ , MCS = 0), and (CBW=160 MHz,  $N_{STS} = 4$ , MCS = 0). Apparently, these configurations are not associated with specific  $N_{STS}$  or CBW values. Our investigation links these large time increases to jumps in the number of OFDM subcarriers  $N_{SC}$ . More specifically, at these triggering configurations,  $N_{SC}$  increases by multiples of 512, *i.e.*, the  $N_{SC}$  changes are  $384 \rightarrow 640$ ,  $256 \rightarrow 512$ ,  $768 \rightarrow 1024$ ,  $512 \rightarrow 1024$ ,  $1024 \rightarrow 1536$  and  $1536 \rightarrow 2048$ . We believe that these time increases triggered by values of  $N_{SC} = 512n$  are related to certain low-level details of the compilation optimization, such as the capacity of the per-SIMD instructions. It is also one of our future goals to determine the reason for this observation and further optimize the baseband performance.

Finally, Figs. 24 and 25 compare the signal encoding and decoding times *w.r.t.* the Wi-Fi protocol and coding scheme.

We make two main observations based on the results. First, we observe only slight time consumption differences among the different protocols. These slight differences are mainly caused by protocol overhead, such as a longer and more complex SIG field in the preamble. Second, in terms of coding, the complexity of LDPC coding is much higher than that of BCC. In both figures, LDPC coding takes approximately 1.5-3x more time than BCC. In addition to the longer codec time,

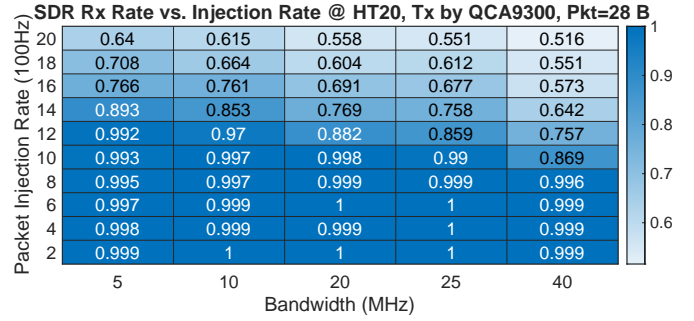


Fig. 26. SDR real-time Rx rates under varying injection rates and bandwidths. The Rx end had 1 Rx antenna, and the injected packets were 32 B CSI Probing Frames with  $N_{STS} = 1$  and MCS=4.

LDPC coding also shows a larger variance in the codec time. Based on this evaluation, we recommend that PicoScenes users prioritize BCC, considering both performance and compatibility issues. The compatibility issue is that the IWL5300 does not support LDPC coding.

2) *Stage 2: Real-time performance evaluation:* Since the primary service goal of PicoScenes is Wi-Fi sensing, in this evaluation, we focused on answering one of the most important and basic questions: *how fast can PicoScenes on SDR measure CSI in real time?* We sought to answer this question from three orthogonal perspectives: first, the Rx rate *w.r.t.* the packet injection speed; second, the Rx rate *w.r.t.*  $N_{STS}$  and  $N_{ANT}$ ; and third, the Rx rate *w.r.t.* the bandwidth and CBW.

*Performance Evaluation Setup:* In the first and second tests, we used the QCA9300 to inject packets at high frequency and used two USRP X310s as our SDR frontend. In the third test, we used two USRP X310s as the Tx and Rx ends. In these tests, each X310 was equipped with two UBX-160 daughterboards; both X310s were connected to the host computer via an Intel X710 Quad Port 10 Gb Ethernet Adapter.

*T1: Performance w.r.t. the packet injection rate:* In the first evaluation, both the Tx and Rx were operated with one radio chain, *i.e.*,  $N_{STS} = 1$  and  $N_{ANT} = 1$ . The baseband bandwidths on both ends were scanned from 5 to 40 MHz. At each bandwidth, the injection rate of the Tx was scanned from 200 to 2000 Hz, and at each injection rate, the Tx injected 10000 32 B CSI Probing Frames and we logged the corresponding Rx rate.

As shown in Fig. 26, the results are *remarkable*. At the standard 20 MHz bandwidth, PicoScenes on SDR achieved a 99.8% Rx rate at a 1000 Hz injection rate, and even at the 2x faster 40 MHz bandwidth, it still achieved a 99.6% Rx rate at an 800 Hz injection rate. This high performance is groundbreaking. To the best of our knowledge, this is the first time that *SDR devices have achieved CSI measurement performance comparable to that of COTS Wi-Fi NICs*.

Besides the excellent figures, the results show predictable performance trends. As the packet injection rate or the bandwidth increases, the baseband computational workload intensifies. When the injection rate is above approximately 1100 Hz, the decoding speed can no longer keep up with the injection rate. To prevent buffer overflow, the baseband buffer must drop

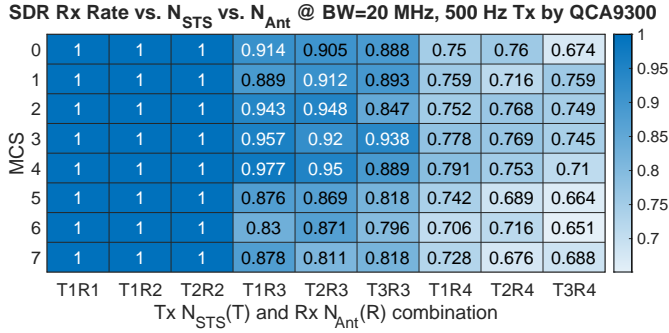


Fig. 27. SDR real-time Rx rates under different Tx  $N_{STS}$ , MCS and Rx  $N_{ANT}$  settings. The Tx end, a QCA9300 NIC, injected 32B CSI Probing Frames at 500 Hz. Both the Tx and Rx were operated at a 20 MHz bandwidth.

signals, which eventually leads to a decline in the Rx rate. Interestingly, as the bandwidth increases by 8x from 5 MHz to 40 MHz, the Rx rate shows only a 10-25% decline. This is due to the highly efficient packet detection implementation, which quickly filters out non-packet segments in the signals.

#### T2: Performance w.r.t. modulation and number of antennas:

In this evaluation, we tested the real-time performance of PicoScenes on SDR w.r.t. the Tx  $N_{STS}$ , Rx  $N_{ANT}$  and MCS settings. We enumerated a total of 72 configurations corresponding to  $N_{STS} \in \{1 - 3\}$ ,  $N_{ANT} \in \{1 - 4\}$ , and  $MCS \in \{0 - 7\}$ . The Tx end, a QCA9300 NIC, injected 10000 32 B CSI Probing Frames in each channel configuration. The injection rate was 500 Hz, which is acceptable for most Wi-Fi sensing research. For the SDR Rx end, to provide up to 4 Rx radio chains, we used the UHD `uhd::usrp::multi_usrp` API to combine two USRP X310 devices into one virtual USRP device equipped with 4 independent radio chains.

Fig. 27 shows the Rx rates. First, we see a 100% Rx rate for the case of  $N_{ANT} \leq 2$  and  $N_{STS} \leq 2$ , i.e., 2x2 MIMO with a 500 Hz injection rate. This further convinces us that SDR is now a competitive alternative to COTS NICs in Wi-Fi sensing research. Second, compared to the  $N_{ANT} \leq 2$  cases, we see an approximately 15% to 25% Rx rate drop in the  $N_{ANT} = 3$  and  $N_{ANT} = 4$  cases. This is mainly due to the 3x and 4x raw baseband signal input rates, which exceed the decoding speed and lead to signal dropping. Third, regarding  $N_{STS}$ , we see that every increase in  $N_{STS}$  by 1 brings about a 5% loss in the Rx rate. This is due to the longer baseband processing required for MIMO decoding. Finally, from the MCS perspective, we strangely find that in cases with  $MCS=0$ , the most resilient MCS level, performance is poor and is sometimes even the worst. This is because  $MCS=0$  produces the longest baseband signal, which is more prone to be dropped. By contrast, a higher MCS index results in shorter packet signals and therefore yields a better Rx rate.

#### T3: Performance w.r.t. the bandwidth and CBW:

In this test, to evaluate the performance throughout a wide bandwidth and CBW range, we used two USRP X310s as both the Tx and Rx ends. We enumerated 56 configurations of the bandwidth, CBW and coding scheme, including bandwidths of up to 200 MHz<sup>9</sup>, CBWs of up to 160 MHz and both BCC and LDPC

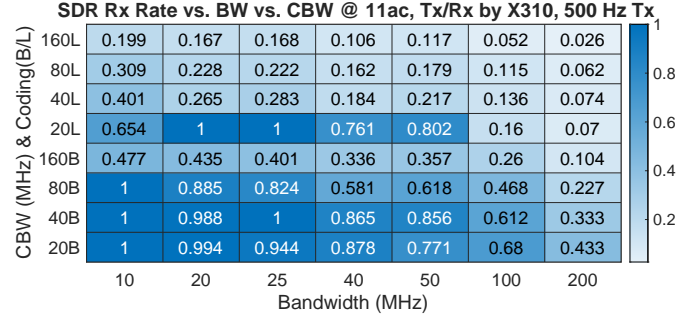


Fig. 28. SDR real-time Rx rates under different bandwidths and CBWs. Both the Tx and Rx were USRP X310s with two UBX-160 daughterboards. The Tx end injected 32 B CSI Probing Frames in the 802.11ac BCC and LDPC formats. The injection rate was 500 Hz. 20B/20L and similar labels on the Y-axis denote a 20/40/80/160 MHz CBW with BCC/LDPC coding.

coding. In each configuration, we used PicoScenes to inject 10000 CSI Probing Frames in the 802.11ac format at a fixed 500 Hz injection rate and logged the Rx rate.

The results are shown in Fig. 28. We first observe a gradual declining trend of the Rx rate with increasing bandwidth and CBW. The reason for the CBW-related Rx rate decline is that a higher CBW leads to longer OFDM symbols and, inevitably, a larger computational overhead. It slows the processing speed and leads to signal dropping. Second, the figure shows that the Rx rate with BCC is roughly 3x higher than the LDPC-based rate, which is consistent with the loopback test presented in Fig. 25. This is because the 3x longer decoding time of the LDPC codec causes an approximately 3x higher signal drop rate. Third, if we look at the Rx rates under high-bandwidth conditions, the results are remarkable. For example, a 20 MHz CBW with BCC yields a 43.3% Rx rate at the 200 MHz baseband, which can be equivalently interpreted as maximal 200 Hz CSI sampling over the 200 MHz wide bandwidth. We believe this high-bandwidth performance will push Wi-Fi sensing to a higher accuracy.

In addition to the performance evaluation, the CSI measurements themselves are also important. Fig. 29 plots the CSI measurements from the 80 MHz CBW test group. In the 80 MHz CBW configuration, the CSI includes a total of 245 subcarriers, comprising 234 data subcarriers, 8 pilot subcarriers and 3 interpolated subcarriers around the DC. The most prominent observation is the CSI measured at a 200 MHz bandwidth. It shows the familiar horizontal S-shaped phase distortion, which was previously identified as Type I distortion. The phase distortion observed at this bandwidth corroborates our conjecture that the baseband filter causes the CSI distortion. Specifically, the RF frontend we used in this evaluation, i.e., a UBX-160 daughterboard [48] installed on a USRP X310, has a smaller bandwidth (160 MHz) than the maximal bandwidth (200 MHz) of the X310 motherboard. Accordingly, for transmission at less than a 160 MHz bandwidth, the response of the baseband filter is flat; however, for bandwidths near or above 160 MHz, the filter shows significant influence. Another point worth noting is that if we look carefully at the magnitude response, we observe that the magnitude response at a 20/40 MHz bandwidth has a much

<sup>9</sup>The maximum bandwidth supported by the USRP X310 is 200 MHz.

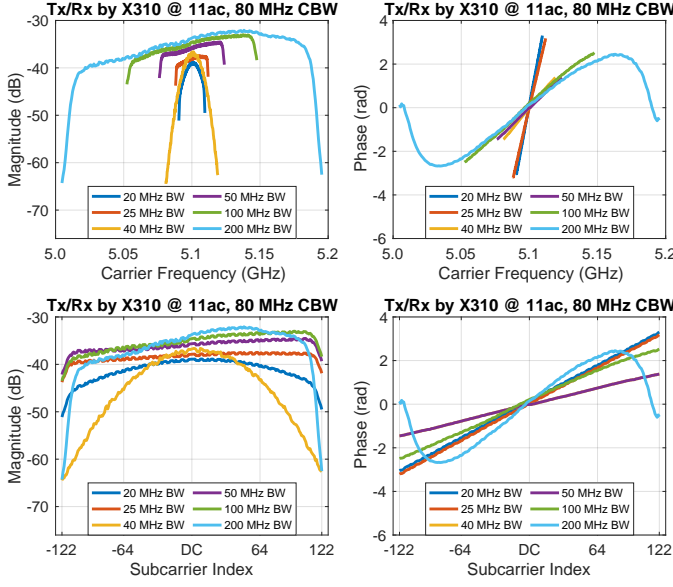


Fig. 29. CSI (magnitude and phase response) measured by the USRP X310 under different bandwidths. Both the Tx and Rx were USRP X310s with two UBX-160 daughterboards. The Tx end injected 32 B CSI Probing Frames using the 802.11ac protocol with an 80 MHz CBW. At both ends, the bandwidth was scanned from to 200 MHz. The top and bottom figures show the CSI in the spectrum view and the subcarrier view, respectively.

stronger roll-off than the response at other bandwidths. This is due to the cascaded integrated comb (CIC) roll-off fading caused by odd-number downclocking. In our case, we use multiples of 5 (10 and 5) to downclock the master clock rate of 200 MHz to 20 and 40 MHz, respectively. Interestingly, this fading is another demonstration of the influence of baseband filters.

### C. Summary of evaluations

Here, we briefly summarize the extensive evaluations, of which many of the results are state of the art.

- The QCA9300 yielded superior link quality even under 3x3 MIMO and the 2x faster 40 MHz bandwidth over the 2.4 GHz full-spectrum. The QCA9300 also achieved reliable single-input-single-output (SISO) communication at bandwidths as low as 2.5 MHz and up to 70 MHz.
- We presented a design for a 27-NIC Wi-Fi sensing array and evaluated its concurrent CSI measurement performance. It yielded a >95% Rx success rate under an 8 kHz packet injection rate.
- We explored the limit of the CSI measurement rate for a single NIC. The CSI measurement rate of the QCA9300 can reach the theoretical limits of 20 kHz and up to 40 kHz for 20 and 40 MHz bandwidths, respectively.
- We evaluated the in situ encoding and decoding performance of PicoScenes on SDR. It was shown to support the most of baseband configurations, such as the 802.11a/g/n/ac/ax protocols, 20/40/80/160 MHz CBWs,  $MCS \leq 10$ ,  $N_{STS} \leq 4$ ,  $N_{ANT} \leq 4$  and the BCC and LDPC coding schemes.
- We evaluated the CSI measurement performance of PicoScenes on SDR in real-world scenarios. It yielded 1

kHz and 800 Hz CSI measurements under bandwidths of 20 and 40 MHz, respectively. It supported up to 4 Rx antennas and Tx/Rx bandwidths of up to 200 MHz. We also demonstrated the first CSI measurement at an 80 MHz CBW and a 200 MHz bandwidth.

## VII. DISCUSSION & FUTURE WORK

In this work, we have focused on hardware baseband design, CSI distortion, and the release of the PicoScenes Wi-Fi sensing system. There are several directions in which our work can be further extended, which we discuss below.

*Deeper exploration of COTS hardware and drivers.* Although some important features have been made available for the QCA9300, many aspects of its drivers have not been thoroughly explored, such as radio calibration, Tx power compensation, and raw ADC/DAC access. In future work, we will continue to explore the QCA9300 hardware design and driver modification. We hope to add more powerful features for the QCA9300 and other CSI-available COTS Wi-Fi NICs.

*Support for more hardware:* PicoScenes provides a publicly available Wi-Fi baseband implementation; however, expensive hardware remains a hindrance for SDR-based Wi-Fi sensing. To solve this problem, we are working on providing support for low-cost AD9361-based SDR devices, such as limeSDR [49], which are more affordable and cost-effective.

*Faster execution of PicoScenes on SDR:* PicoScenes on SDR, at its core, is still a single-threaded implementation and thus cannot fully utilize the available computational resources. By parallelizing the decoding flow, the decoding performance can be greatly improved. Another breakthrough is expected to be hardware-based acceleration. We hope to use high-level synthesis (HLS) technology to ease the C++ to Verilog/VHDL language translation.

## VIII. CONCLUSION

This paper accomplishes three tasks, with the aim of eliminating the key barriers to Wi-Fi sensing research. An in-depth study of the baseband design of the QCA9300 helps us characterize the CSI distortion. The lessons learned provide us with a paradigm from which to speculate how other Wi-Fi NICs operate. We also propose a trivial distortion removal method. Regarding hardware inadequacies, we reintroduce both the QCA9300 NIC and SDR as the best hardware for Wi-Fi sensing. We enable over-GHz spectrum access on the QCA9300 and develop a high-performance software implementation of the Wi-Fi baseband. We release the PicoScenes software. It supports concurrent packet injection and CSI measurement based on QCA9300, IWL5300 and SDR hardware. It is architecturally flexible and allows users to develop their own measurement plugins. Extensive evaluations verify the performance of PicoScenes and yield many state-of-the-art results. We believe that PicoScenes, as a groundbreaking measurement software platform, will significantly benefit the entire Wi-Fi sensing research community.

## REFERENCES

- [1] F. Hong, X. Wang, Y. Yang, Y. Zong, Y. Zhang, and Z. Guo, "Wfid: Passive device-free human identification using wifi signal," in *Proceedings of the 13th International Conference on Mobile and Ubiquitous Systems: Computing, Networking and Services (MOBIQUITOUS'16)*, 2016, pp. 47–56.
- [2] L. Wang, K. Sun, H. Dai, A. X. Liu, and X. Wang, "Witrace: Centimeter-level passive gesture tracking using wifi signals," in *Proceedings of the 15th Annual IEEE International Conference on Sensing, Communication, and Networking (SECON'18)*, 2018, pp. 1–9.
- [3] Y. Bai, Z. Wang, K. Zheng, X. Wang, and J. Wang, "Widrive: Adaptive wifi-based recognition of driver activity for real-time and safe takeover," in *Proceedings of the 39th IEEE International Conference on Distributed Computing Systems (ICDCS'19)*, 2019, pp. 901–911.
- [4] K. Qian, C. Wu, Y. Zhang, G. Zhang, Z. Yang, and Y. Liu, "Widar2.0: Passive human tracking with a single wi-fi link," in *Proceedings of the 16th Annual International Conference on Mobile Systems, Applications, and Services (MobiSys'18)*, 2018, pp. 350–361.
- [5] H. Abdelnasser, K. A. Harras, and M. Youssef, "Ubibreath: A ubiquitous non-invasive wifi-based breathing estimator," in *Proceedings of the 16th ACM International Symposium on Mobile Ad Hoc Networking and Computing (MobiHoc'15)*, 2015, pp. 277–286.
- [6] D. Zhang, Y. Hu, Y. Chen, and B. Zeng, "Breathtrack: Tracking indoor human breath status via commodity wifi," *IEEE Internet of Things Journal*, vol. 6, no. 2, pp. 3899–3911, 2019.
- [7] A. Hanif, M. Iqbal, and F. Munir, "Wispy: Through-wall movement sensing and person counting using commodity wifi signals," in *IEEE SENSORS*, 2018, pp. 1–4.
- [8] Y. Ma, G. Zhou, S. Wang, H. Zhao, and W. Jung, "Signfi: Sign language recognition using wifi," *Proc. ACM Interact. Mob. Wearable Ubiquitous Technol.*, vol. 2, no. 1, pp. 1–21, 2018.
- [9] H. Li, W. Yang, J. Wang, Y. Xu, and L. Huang, "Wifinger: Talk to your smart devices with finger-grained gesture," in *Proceedings of the 2016 ACM International Joint Conference on Pervasive and Ubiquitous Computing (UbiComp'16)*, 2016, pp. 250–261.
- [10] Y. Ma, G. Zhou, and S. Wang, "Wifi sensing with channel state information: A survey," *ACM Comput. Surv.*, vol. 52, no. 3, pp. 1–36, Jun. 2019.
- [11] N. Tadayon, M. T. Rahman, S. Han, S. Valaee, and W. Yu, "Decimeter ranging with channel state information," *IEEE Transactions on Wireless Communications*, vol. 18, no. 7, pp. 3453–3468, 2019.
- [12] I. S. Association, *part 11: Wireless LAN Medium Access Control (MAC) and Physical Layer (PHY) specifications amendment 5: enhancements for higher throughput*, 2011.
- [13] D. Halperin, W. Hu, A. Sheth, and D. Wetherall, "Tool release: Gathering 802.11n traces with channel state information," *ACM SIGCOMM CCR*, vol. 41, no. 1, p. 53, 2011.
- [14] Y. Xie, Z. Li, and M. Li, "Precise Power Delay Profiling with Commodity Wi-Fi," *IEEE Transactions on Mobile Computing*, vol. 18, no. 6, pp. 1342–1355, 2019.
- [15] F. Gringoli, M. Schulz, J. Link, and M. Hollick, "Free your csi: A channel state information extraction platform for modern wi-fi chipsets," in *Proceedings of the 13th International Workshop on Wireless Network Testbeds, Experimental Evaluation & Characterization (WiNTECH'19)*, 2019, pp. 21–28.
- [16] H. Zhu, Y. Zhuo, Q. Liu, and S. Chang, "Splicer: Perceiving accurate csi phases with commodity wifi devices," *IEEE Transactions on Mobile Computing*, vol. 17, no. 9, pp. 2155–2165, 2018.
- [17] J. Xiong, K. Sundaresan, and K. Jamieson, "Tonetrack: Leveraging frequency-agile radios for time-based indoor wireless localization," in *Proceedings of the 21st Annual International Conference on Mobile Computing and Networking (MobiCom'15)*, 2015, pp. 537–549.
- [18] R. Ayyalasomayajula, D. Vasisht, and D. Bharadia, "Bloc: Csi-based accurate localization for ble tags," in *Proceedings of the 14th International Conference on Emerging Networking EXperiments and Technologies (CoNEXT'18)*, 2018, p. 126–138.
- [19] Y. Xie, J. Xiong, M. Li, and K. Jamieson, "md-track: Leveraging multidimensionality for passive indoor wi-fi tracking," in *Proceedings of the 25th Annual International Conference on Mobile Computing and Networking (MobiCom'19)*, 2019, pp. 1–16.
- [20] S. Zhao, Z. Qu, Z. Luo, Z. Lu, and Y. Liu, "Comb decoding towards collision-free wifi," in *Proceedings of the 17th USENIX Symposium on Networked Systems Design and Implementation (NSDI'20)*, Feb. 2020, pp. 933–951.
- [21] J. Gjengset, J. Xiong, G. Mcphillips, and K. Jamieson, "Phaser: Enabling phased array signal processing on commodity wifi access points," in *Proceedings of the 20th Annual International Conference on Mobile Computing and Networking (MobiCom'14)*, 2014, pp. 153–164.
- [22] S. Kumar, S. Kumar, and D. Katabi, "Decimeter-level localization with a single wifi access point," in *Proceedings of the 13th USENIX Symposium on Networked Systems Design and Implementation (NSDI'16)*, 2016, pp. 165–178.
- [23] Z.-P. Jiang, W. Xi, X. Li, S. Tang, J.-Z. Zhao, J.-S. Han, K. Zhao, Z. Wang, and B. Xiao, "Communicating is crowdsourcing: Wi-fi indoor localization with csi-based speed estimation," *Journal of Computer Science and Technology*, vol. 29, no. 4, pp. 589–604, 2014.
- [24] W. Xi, J. Zhao, X.-Y. Li, K. Zhao, S. Tang, X. Liu, and Z. Jiang, "Electronic frog eye: Counting crowd using wifi," in *IEEE INFOCOM 2014-IEEE Conference on Computer Communications*. IEEE, 2014, pp. 361–369.
- [25] M. Kotaru, K. R. Joshi, D. Bharadia, and S. Katti, "Spotfi: Decimeter level localization using wifi," in *Proceedings of the 2015 ACM Conference on Special Interest Group on Data Communication (SIGCOMM'15)*, 2015, pp. 269–282.
- [26] Z. Yang, C. Wu, and Y. Liu, "Locating in fingerprint space: Wireless indoor localization with little human intervention," in *Proceedings of the 18th Annual International Conference on Mobile Computing and Networking (MobiCom'12)*, 2012, pp. 269–280.
- [27] Y. Zheng, G. Shen, L. Li, C. Zhao, M. Li, and F. Zhao, "Travi-navi: Self-deployable indoor navigation system," in *Proceedings of the 20th Annual International Conference on Mobile Computing and Networking (MobiCom'14)*, 2014, pp. 471–482.
- [28] C. Wu, F. Zhang, Y. Fan, and K. J. R. Liu, "Rf-based inertial measurement," in *Proceedings of the ACM Special Interest Group on Data Communication (SIGCOMM'19)*, 2019, pp. 117–129.
- [29] N. Keerativoranan, P. Hanpinitsak, K. Saito, and J. I. Takada, "Analysis of non-intrusive hand trajectory tracking by utilizing micro-doppler signature obtained from wi-fi channel state information," *IEEE Access*, vol. 8, pp. 176 430–176 444, 2020.
- [30] Z. Chen, P. Yang, J. Xiong, Y. Feng, and X. Y. Li, "Tagray: Contactless sensing and tracking of mobile objects using cots rfid devices," in *Proceedings of the 39th IEEE International Conference on Computer Communications (INFOCOM'20)*, 2020, pp. 307–316.
- [31] M. Kotaru and S. Katti, "Position tracking for virtual reality using commodity wifi," in *Proceedings of IEEE International Conference on Computer Vision and Pattern Recognition (CVPR'17)*, 2017, pp. 2671–2681.
- [32] C. Feng, J. Xiong, L. Chang, J. Wang, X. Chen, D. Fang, and Z. Tang, "Wimi: Target material identification with commodity wi-fi devices," in *Proceedings of the 39th IEEE International Conference on Distributed Computing Systems (ICDCS'19)*, 2019, pp. 700–710.
- [33] J. Xiao, H. Li, and Y. Liu, "Wiwrite: Wi-fi based handwriting recognition like playing lego," in *Proceedings of the 28th International Conference on Computer Communication and Networks (ICCCN'19)*, 2019, pp. 1–9.
- [34] J. Xiong and K. Jamieson, "Securearray: Improving wifi security with fine-grained physical-layer information," in *Proceedings of the 19th annual international conference on Mobile computing & networking*, 2013, pp. 441–452.
- [35] Z. Jiang, J. Zhao, X.-Y. Li, J. Han, and W. Xi, "Rejecting the attack: Source authentication for wi-fi management frames using csi information," in *2013 Proceedings IEEE INFOCOM*. IEEE, 2013, pp. 2544–2552.
- [36] P. Xie, J. Feng, Z. Cao, and J. Wang, "Genewave: Fast authentication and key agreement on commodity mobile devices," *IEEE/ACM Transactions on Networking*, vol. 26, no. 4, pp. 1688–1700, 2018.
- [37] Y. Xie, Y. Zhang, J. C. Liando, and M. Li, "Swan: Stitched wi-fi antennas," in *Proceedings of the 24th Annual International Conference on Mobile Computing and Networking (MobiCom'18)*, 2018, pp. 51–66.
- [38] Y. Zhu, Z. Xiao, Y. Chen, Z. Li, M. Liu, B. Y. Zhao, and H. Zheng, "Et tu alexa? when commodity wifi devices turn into adversarial motion sensors," in *Proceedings of the Network and Distributed System Security Symposium (NDSS'20)*, 2020.
- [39] M. Zargari, L. Y. Nathawad, H. Samavati, and et al., "A Dual-Band CMOS MIMO Radio SoC for IEEE 802.11n Wireless LAN," *IEEE Journal of Solid-State Circuits*, vol. 43, no. 12, pp. 2882–2895, 2008.
- [40] S. G. Sankaran, B. J. Zargari, and e. a. L. Y. Nathawad, "Design and Implementation of A CMOS 802.11n SoC," *IEEE Communications Magazine*, vol. 47, no. 4, pp. 134–143, 2009.
- [41] S. Abdollahi-Alibeik, D. Weber, H. Dogan, and et al., "A 65nm dual-band 3-stream 802.11n mimo wlan soc," in *Proceedings of 2011 IEEE*

*International Solid-State Circuits Conference (ISSCC'11)*, 2011, pp. 170–172.

[42] P. J. Husted, T.-F. S. Ng, and Q. A. Inc, “Receiving and transmitting signals having multiple modulation types using sequencing interpolator,” Patent, Aug., 2006.

[43] Linux Wireless Wikipedia, “Atheros Linux wireless drivers – ath9k,” <https://wireless.wiki.kernel.org/en/users/Drivers/ath9k>.

[44] B. Sklar, *Digital Communication: Fundamentals and Applications*. Publishing House of Electronics Industry, 2006.

[45] IEEE LAN/MAN Standard Committee, *IEEE 802.11 Amendment 5 (802.11n): Enhancements for Higher Throughput in Wireless LANs*. IEEE Wireless Communications, Oct. 2009.

[46] Ettus Research, “USRP Hardware Driver and USRP Manual,” <https://files.ettus.com/manual/index.html>.

[47] T. D. Chiueh, P. Y. Tsai, and L. I-Wei, *Baseband Receiver Design for Wireless MIMO-OFDM Communications*, 2012.

[48] Ettus Research, “UBX 10-6000 MHz Rx/Tx (160 MHz, X Series only),” <https://www.ettus.com/all-products/ubx160/>.

[49] Lime Microsystems, “LimeSDR,” <https://limemicro.com/products/boards/limesdr/>.



**Zhiping Jiang** received the PhD degree in computer science from Xi'an Jiaotong University in 2017. He is now an assistant professor at the School of Computer Science and Technology, Xidian University. His research interests include wireless sensing, WiFi/acoustic communication and mobile computing. For more information, please visit <https://zpj.io/>.



content distribution and peer-to-peer networking, and protocol design and performance evaluation of wireless cloud computing and edge computing.



**Xincheng Ren** received the BS degree in oil-gas storage and transportation engineering from Changzhou University in 2019. He is currently a graduate student the School of Computer Science and Technology, Xidian University. His research interests include Wi-Fi sensing and agile baseband signal processing.



**Dongtao Lv** received the BS degree in communication engineering from Xi'an University of Science and Technology in 2019. He is currently a graduate student the School of Computer Science and Technology, Xidian University. His research interests include agile baseband signal processing and heterogenous DSP acceleration.



**Han Hao** received the BS degree in electrical engineering from North China Electric Power University in 2019. He is currently a graduate student with the School of Computer Science and Technology, Xi'an Jiaotong University. His research interests include cross-protocol communication, pervasive computing and wireless networks.



**Jing Wang** received the BS degree in telecommunication engineering from Shenzhen University in 2020. She is currently a graduate student the School of Computer Science and Technology, Xidian University. Her research interests include wireless sensing, wireless communication and mobile computing.



**Kun Zhao** received his Ph.D degree on Computer Science from Xi'an Jiaotong University in 2019. He is currently an assistant professor at the School of Computer Science and Technology, Xi'an Jiaotong University. His research interests include signal processing, wireless security, and federated learning.



**Wei Xi** received his Ph.D degree on Computer Science from Xi'an Jiaotong University in 2014. He is currently an associate professor at the School of Computer Science and Technology, Xi'an Jiaotong University. His research interests include wireless networks, mobile computing, and AI.



**Yueshen Xu** received the PhD degree from Zhejiang University, and was a co-trained Ph.D. student with the University of Illinois, Chicago. He is now an associate professor with the School of Computer Science and Technology, Xidian University. His research interests include recommender systems, mobile computing, and service computing.



**Rui Li** received the PhD degree in computer science from Xi'an Jiaotong University in 2014. He is now an associate professor at the School of Computer Science and Technology, Xidian University, China. His research interests include smart sensing, radar imaging and pervasive computing.